
Article:
Paraskevoulakos, C., Forna-Kreutzer, J.P., Hallam, K.R. et al. (9 more authors) (2021) Investigating the microstructure and mechanical behaviour of simulant "lava-like" fuel containing materials from the Chernobyl reactor unit 4 meltdown. Materials & Design, 201. 109502. ISSN 0264-1275

https://doi.org/10.1016/j.matdes.2021.109502

Materials and Design 201 (2021) 109502

Contents lists available at ScienceDirect

Materials and Design

journal homepage: www.elsevier.com/locate/matdes

Investigating the microstructure and mechanical behaviour of simulant "lava-like" fuel containing materials from the Chernobyl reactor unit 4 meltdown

C. Paraskevoulakos [a,*], J.P. Forna-Kreutzer [b], K.R. Hallam [a], C.P. Jones [a], T.B. Scott [a], C. Gausse [c], D.J. Bailey [c], C.A. Simpson [d], D. Liu [e], C. Reinhard [f], C.L. Corkhill [c], M. Mostafavi [d]

[a] Interface Analysis Centre, School of Physics, University of Bristol, Bristol BS8 1TL, UK
[b] Bristol Composites Institute, Department of Aerospace Engineering, University of Bristol, Bristol BS8 1TR, UK
[c] Immobilisation Science Laboratory, Department of Materials Science and Engineering, University of Sheffield, Sheffield S13JD, UK
[d] Department of Mechanical Engineering, University of Bristol, Bristol BS8 1TR, UK
[e] School of Physics, University of Bristol, Bristol BS8 1TL, UK
[f] Diamond Light Source, Harwell Science and Innovation Campus, Didcot OX11 0DE, UK

HIGHLIGHTS

- Chernobyl "lava-like" fuel-containing material (LFCM) can be classified as brittle.
- Porosity varies depending on the type of the LFCM (brown or black).
- The range of Young's modulus for the Chernobyl lavas varies between 5 GPa and 16 GPa.
- The stiffness of brown lava is almost 2.5 time greater than that of black lava.

GRAPHICAL ABSTRACT

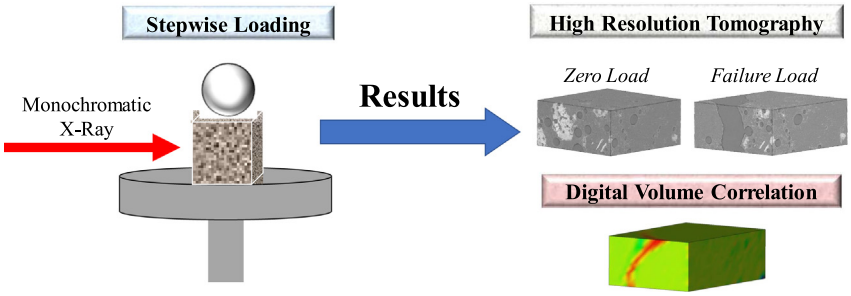

ARTICLE INFO

Article history:
Received 10 October 2020
Received in revised form 28 December 2020
Accepted 16 January 2021
Available online 20 January 2021

Keywords:
Synchrotron radiation computed tomography
Digital volume correlation
Mechanical properties
Fracture
Chernobyl "lavas"

ABSTRACT

Decommissioning of the damaged Chernobyl nuclear reactor Unit 4 is a top priority for the global community. Before such operations begin, it is crucial to understand the behaviour of the hazardous materials formed during the accident. Since those materials formed under extreme and mostly unquantified conditions, modelling alone is insufficient to accurately predict their physical, chemical and, predominantly, mechanical behaviour. Meanwhile, knowledge of the mechanical characteristics of those materials, such as their strength, is a priority before robotic systems are employed for retrieval and the force expected from them to be exerted is one of the key design questions. In this paper we target to measurement of the standard mechanical properties of the materials formed during the accident by testing small-scale, low radioactivity simulants. A combined methodology using Hertzian indentation, synchrotron X-ray tomography and digital volume correlation (DVC), was adopted to estimate the mechanical properties. Displacement fields around the Hertzian indentation, performed in-situ in a synchrotron, were measured by analysing tomograms with DVC. The load applied during the indentation, combined with full-field displacement measured by DVC was used to estimate the mechanical properties, such as Young's modulus and Poisson's ratio of these hazardous materials.

* Corresponding author.
E-mail addresses: cp13846@bristol.ac.uk (C. Paraskevoulakos), jp.fornakreutzer@bristol.ac.uk (J.P. Forna-Kreutzer), k.r.hallam@bristol.ac.uk (K.R. Hallam), cj0810@bristol.ac.uk (C.P. Jones), t.b.scott@bristol.ac.uk (T.B. Scott), c.gausse@sheffield.ac.uk (C. Gausse), d.j.bailey@sheffield.ac.uk (D.J. Bailey), c.simpson@bristol.ac.uk (C.A. Simpson), d.liu@bristol.ac.uk (D. Liu), christina.reinhard@diamond.ac.uk (C. Reinhard), c.corkhill@sheffield.ac.uk (C.L. Corkhill), m.mostafavi@bristol.ac.uk (M. Mostafavi).

https://doi.org/10.1016/j.matdes.2021.109502

1. Introduction

On 26th April 1986, a severe nuclear accident occurred at Unit 4 of the Chernobyl nuclear reactor during an experimental power failure test. The explosion and subsequent fire released a significant amount of radioactive solid and gaseous products into the surrounding environment, while the reactor core was decimated [1,2]. Temperatures far exceeded 2000 °C prior to the explosion, leading to reactions between the UO_2 fuel and the zircaloy cladding [3,4]. The fuel-cladding melt further interacted with neighbouring reactor components, including stainless steel and construction materials (concrete, sand and serpentinite) [2]. These molten materials formed a "lava-like" mixture, which dispersed within the reactor, penetrating premises of the structure, eventually solidifying in the basement levels. The solid heterogeneous mixture is known as the Chernobyl "lava" or "lava-like" fuel containing materials (LFCM).

Immediately after the accident occurred, a massive steel and concrete structure was assembled to cover the building where the Unit 4 ruined reactor was located. This structure, known as the Chernobyl nuclear power plant sarcophagus, was designed to limit the post-accident radioactive contamination. However, within the first of decade of operation the structure had severely deteriorated, allowing water to access the inside of the ruined reactor. As a result, radioactive aerosol particles have formed, posing serious threats of airborne contamination and respirable hazards around the area [5,6]. Therefore, a decision for replacement was adopted. In November 2016, operations to replace the old sarcophagus with a new safe confinement were successfully completed.

Today, almost 35 years after the nuclear accident occurred, LFCM still resides in the vicinity of the damaged reactor Unit 4. It is estimated that the accumulated volume of the material exceeds 192 m^3 (~1250 t) [2,7]. The new safe confinement now allows for a robust plan for plant decommissioning, including the dismantling of the ruined reactor Unit 4 and the surrounding "lava". The total clean-up operations and complete decommissioning of the facilities are expected to last until at least 2065.

The extreme high-dose environment within the damaged Unit 4 reactor requires the development and manufacturing of specialised robotic systems to retrieve the LFCM. Successful and safe decommissioning is directly linked with zero risk to material integrity during lift-out. Therefore, knowledge of the physical, chemical and, predominantly, mechanical properties of the material to be retrieved is key for appropriate design of the robotic systems.

Due to high radioactivity in the vicinity of the ruined reactor, it is next-to-impossible to carry out any standard mechanical testing on real samples. Further complications arise from their complex and heterogeneous microstructures that makes single measurements of properties carried out on safe, small-scale specimen testing non-representative of the bulk properties.

Up until today, only one successful attempt to retrieve Chernobyl "lava" has been reported. In 1990, scientists of the V.G. Khlopin Radium Institute (KRI), who took part in the investigations performed immediately after the accident, managed to manually collect samples of the Chernobyl LFCM, and successfully transport it to Leningrad (now St. Petersburg) in 1990 [2]. These samples remain the only pieces of real Chernobyl "lava" in the world that are available for experiments [2]. Thus, since real Chernobyl LFCM is inaccessible and dangerous to handle, it is necessary to examine simulant material for mechanical testing as a feasible method to indirectly determine properties of LFCM. Successful attempts to synthesise materials resembling the formation process and microstructure of the Chernobyl "lava" have been already undertaken [7,8]. The relevant studies describe how to replicate the meltdown conditions as accurately as possible and produce a simulant material to be used for characterisation and testing. To the best of our knowledge, research focusing on mechanical testing of real Chernobyl "lava" samples or simulant materials has not yet been published until today.

The results of an experimental programme launched to investigate the mechanical properties of simulant Chernobyl LFCM samples are discussed in this paper. A methodology including synchrotron X-ray computed tomography (XCT) combined with digital volume correlation (DVC) was adopted to reveal and quantify internal microstructural changes on samples subjected to external loading. XCT is a non-destructive imaging technique, based on acquiring 2D radiographs through an object at numerous projections and then, computationally reconstructing the relevant 3D image. DVC is a powerful technique used to produce 3D full-field internal displacement and strain data from input image packages displaying a gradually-deformed object subjected to time-dependent processes [9–12]. The ability to monitor deformation in the core of the material being probed enables determination of the relationship between microstructure and mechanical behaviour at the macro-scale. This methodology has been successfully employed by researchers investigating the mechanical behaviour of mostly ductile but also quasi-brittle materials [13–17]. We employed this technique to evaluate the properties of LFCM-simulant materials. 3D tomograms were acquired at different stages of Hertzian indentation loading. These tomograms were used as the input datasets to employ DVC analysis and subsequently quantify a wide variety of microstructural changes occurring as load increased. Correlating the displacement calculated via DVC with the corresponding load values is a method to determine the material strength (load bearing capacity) and principal mechanical properties including Young's modulus and Poisson's ratio.

2. Experiment

2.1. Materials and sample preparation

Investigations conducted after the Chernobyl accident revealed the presence of several different Chernobyl "lava" varieties [1,18]. Among those, black and brown LFCM are the most common. The colour differences are attributed to radiation defects and elemental composition of the materials. Brown colour is associated with the presence of zirconium in uranium phases, while the black colour is an indication of uranium dissolution in the glass matrix [2]. Detailed elemental composition of black and brown LFCM samples collected from KRI in 1990 can be found in the literature [2].

Since access to real material for mechanical testing was not feasible, LFCM-simulant samples that accurately replicate those characterised at the KRI were produced based on previously developed work, full details of the synthesis are given elsewhere [3,7,8,18,19]. Briefly, stoichiometric amounts of: SiO_2; $CaCO_3$; ZrO_2; Na_2CO_3; $BaCO_3$; $Al(OH)_3$; Mn_2O_3; Fe/Cr_{18}/Ni_{10}/Mo_3; $Mg(OH)_2$ and UO_2 were intimately mixed prior to heating at 1500 °C for 4 h, before lowering the temperature to 720 °C for 72 h under a reducing atmosphere (95% H_2-N_2 gas). Slow cooling analogous to Chernobyl conditions was enabled by use of a slow cooling profile of 1 °C min^{-1} from 1500 °C to 720 °C. X-ray diffraction (XRD) analysis performed on samples produced under the same process revealed the full range of U—Zr mixed crystalline phases [$(U_{1-x}Zr_x)O_2$, $(Zr_{1-x}U_x)O_2$ and $(Zr_{1-x}U_x)SiO_4$] [7], dispersed within a porous calcium aluminosilicate glass matrix, also containing uranium. For full characterisation and synthesis details for both brown and black LFCM, the reader is directed to [7,8].

2.2. Mechanical loading

Hertzian indentation was selected as the most appropriate loading technique considering the mm-scale size of the samples and based on our previous studies of brittle and quasi-brittle materials [14,20]. Steel holders were machined to retain 5 mm diameter ZrO_2 spheres, acting as indenters. A custom-designed and in-house built mechanical jig (Fig. 1) was used to retain samples during indentation and imaging.

Stepwise mechanical loading, coupled with in situ high-resolution synchrotron XCT, was conducted on beamline I12 at Diamond Light Source (DLS) [21]. Following DLS radiation safety rules and policies, the jig contained three barriers between the radioactive sample and

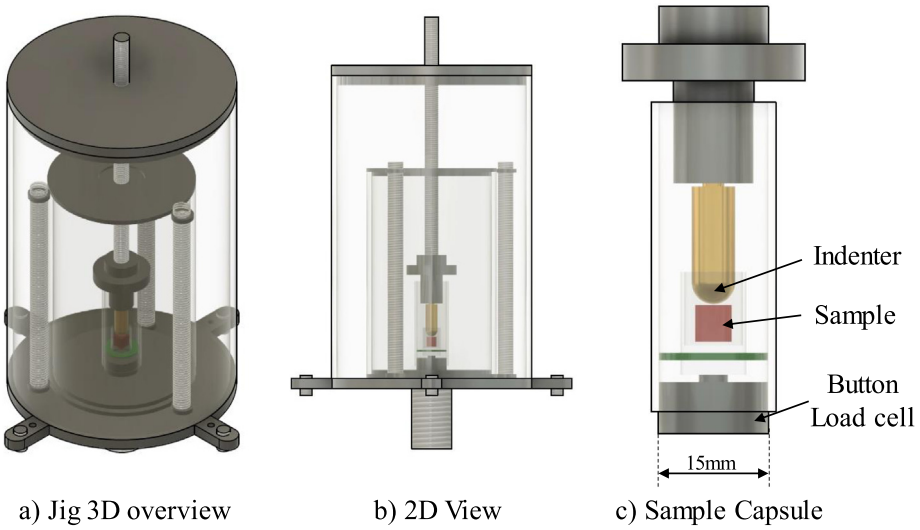

Fig. 1. Schematic of jig built to perform Hertzian indentation loading on LFCM-simulant samples.

the laboratory environment. A miniature button-type load cell was used to measure the compressive reaction force in situ with a 2 s polling interval. External force was applied to the sample manually by rotating a metallic rod attached to the indenter and aligned with the sample holder and the load cell button.

Time restrictions related to synchrotron beamtime availability only allowed investigation of two samples: one black LFCM simulant; one brown LFCM. Experiment feasibility requirements and radioactivity handling limits enforced minimising the size of the samples.

2.3. Synchrotron X-ray tomography

The DLS I12 beamline [21] was used to perform in situ XCT scans on the two samples at different stages of Hertzian indentation loading due to the combination of high flux and energies provided. The monochromatic X-ray beam was tuned at 101.97 keV. Camera optics with field-of-view: 8.0 mm × 7.0 mm and, resolution: 3.25 μm/pixel were used to encompass the entire sample volume. The exposure time was 0.4 s, with 3000 projections acquired per scan (total scan time: 20 min). Reconstruction of the data was performed using the open-source software Savu [22]. Data visualisation and analysis software Avizo [23] was subsequently used for further data processing including 3D visualisation, volume/length measurements and material segmentation.

2.4. Experimental procedure

The loading sequence used during stepwise mechanical loading was selected for each sample based on ex-situ trials. Immediately after the pre-planned value for the applied load was recorded, XCT scans were performed. The ZrO_2 indenter remained in contact with the sample during scanning under an applied load. The first scan prior to loading, and the last scan after sample failure, were performed with the indenter retracted. The force applied on the load cell was continuously monitored. Table 1 summarises all the actions performed in sequence for black and brown LFCM simulant samples. It is important to mention that the load values given in Table 1 refer to the initial-maximum load recorded per cycle. Immediately after reaching the targeted load value, force relaxation started, and the recorded values began to decrease. Thus, the load during the XCT scans was lower than the initial targeted value as given in Table 2.

3. Analysis and results

3.1. Mechanical behaviour

The load paths followed for the two samples (black LFCM; brown LFCM), as recorded throughout the entire experimental period - including both loading and subsequent scanning processes - are presented in Fig. 2.

The black LFCM simulant sample failed during the fourth loading cycle, up to 130 N. A sudden drop of the load was recorded immediately after 127 N. The brown LFCM specimen exhibited a different behaviour since it failed during scanning after the second loading cycle was completed. The "load plateau", which is observed in the graphs (Fig. 2) after each peak load condition was the period when scans were performed.

3.2. Visualisation and segmentation

Fig. 3 illustrates one representative cropped 2D slice for each of the two samples tested. The multiphase nature of the samples is evident.

Table 1
Action sequences performed for the two samples investigated.

Black LFCM	
Step 1	XCT scan at zero loading
Step 2	Load set at 20 N – XCT scan
Step 3	Load set at 50 N – XCT scan
Step 4	Load set at 80 N – XCT scan
Step 5	Load set at 130 N – **Sample failed at 127 N** – Post failure XCT scan
Brown LFCM	
Step 1	XCT scan at zero loading
Step 2	Load set at 20 N – XCT scan
Step 3	Load set at 50 N – XCT scan
Step 4	**Sample failed during scanning** – Post failure XCT scan

Table 2
Load variation during scanning for samples tested.

Initial load (N)	Load at beginning of scan (N)	Load at end of scan (N)
Black LFCM		
20	10.85	10.63
50	41.01	36.96
80	71.42	66.07
130	45.66	44.13
Brown LFCM		
20	15.84	14.56
50	43.03	40.32
–	3.4	3.3

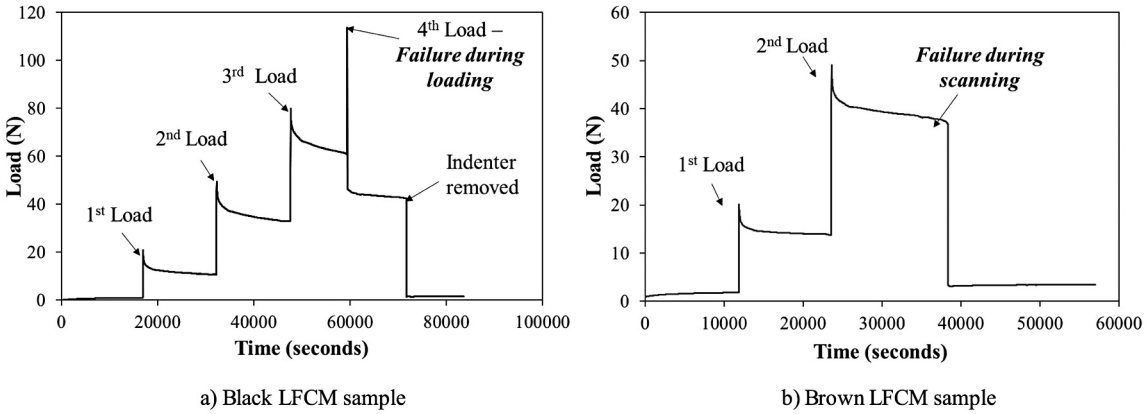

Fig. 2. Load paths recorded during indentation and synchrotron XCT for the two sample materials tested on the DLS I12 beamline.

In situ phase characterisation work was not performed due to time limitations and therefore phase identification is based on the relevant available literature. The bright spots/areas are attributed to high-density Uranium-rich phases. Pores of various sizes are also observed. Based on the different image gray-scale ranges, segmentation of each separate phase was performed, enabling both qualitative and quantitative analysis. The threshold values separating the different phases in the gray-scale intensity range were determined using the "Line-Probe" module in Avizo [23]. A typical segmentation process is illustrated in Fig. 4. Characteristic 2D XCT slices for each of the materials tested are presented, along with the corresponding post-segmentation individual phases, which are shown in white colour.

U-rich phases are assumed to include the range of $(U_{1-x}Zr_x)O_2$ crystallites where the value of x is less than 0.1, while Zr-rich phases contain little or no U, being monoclinic $(Zr_{1-x}U_x)O_2$ (where $x < 0.1$) or zircon, $(Zr_{1-x}U_x)SiO_4$ (where $x < 0.1$). Fe-rich phases, present as small particles from the inclusion of stainless steel in the "lava" composition, are difficult to differentiate from Zr given their similar density (7.84 g cm^{-3} and 6.49 g cm^{-3} for Fe and Zr, respectively), thus they have been grouped together. It should be noted that previous analysis of these materials showed the occurrence of Fe-particles to be low, at ~ < 1 vol%, therefore, the majority of the phases shown in Fig. 4 iv and viii are likely to be Zr-rich.

3D models were also built, as shown in Fig. 5. Cuboid regions were selected from the original samples for 3D model rendering (65% to 85% of the entire volume) to reduce computational time. The segmentation enabled quantification of the contained phase volumes in both samples. Using Avizo segmentation and analysis tools, general porosity, pore size distribution, U-rich and Fe/Zr-rich phase volume fractions were determined using the pre-loaded datasets; results are presented in Fig. 6. It is observed that the brown LFCM sample exhibited a slightly larger U-rich phase volume fraction (2.8%) than did the black LFCM (2.2%). It is also interesting to note that the brown LFCM sample porosity was almost double that of the black LFCM. A similar observation can be made for the Zr/Fe-rich medium density phase volumes. The volume fraction of Zr/Fe-rich phases contained in the brown LFCM sample (16%) is almost double that contained in the black LFCM volume (7.7%). The evolution of structural degradation was monitored as load increased up to failure. Characteristic 3D tomogram screenshots are shown in Fig. 7 for the samples investigated. The load values reported beneath each tomogram correspond to the average load value recorded during the relaxation-scanning process (Table 2). Yellow arrows point at cracks formed due to excessive loading. The isolated crack volume network after failure is shown in Fig. 8 to enable optimum visualisation. The tomograms revealed a single crack having formed in each of the

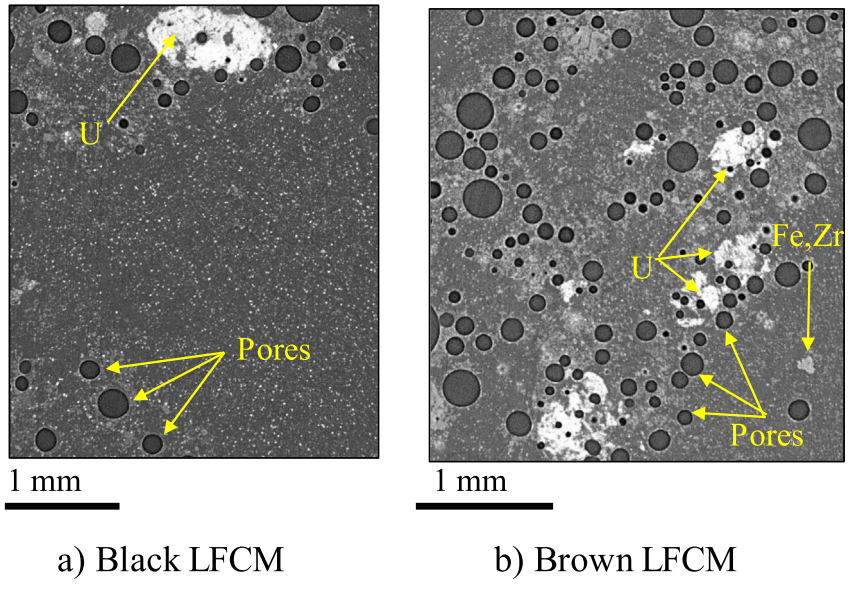

Fig. 3. Representative cropped 2D XCT slices demonstrating the multiphase nature of the sample materials.

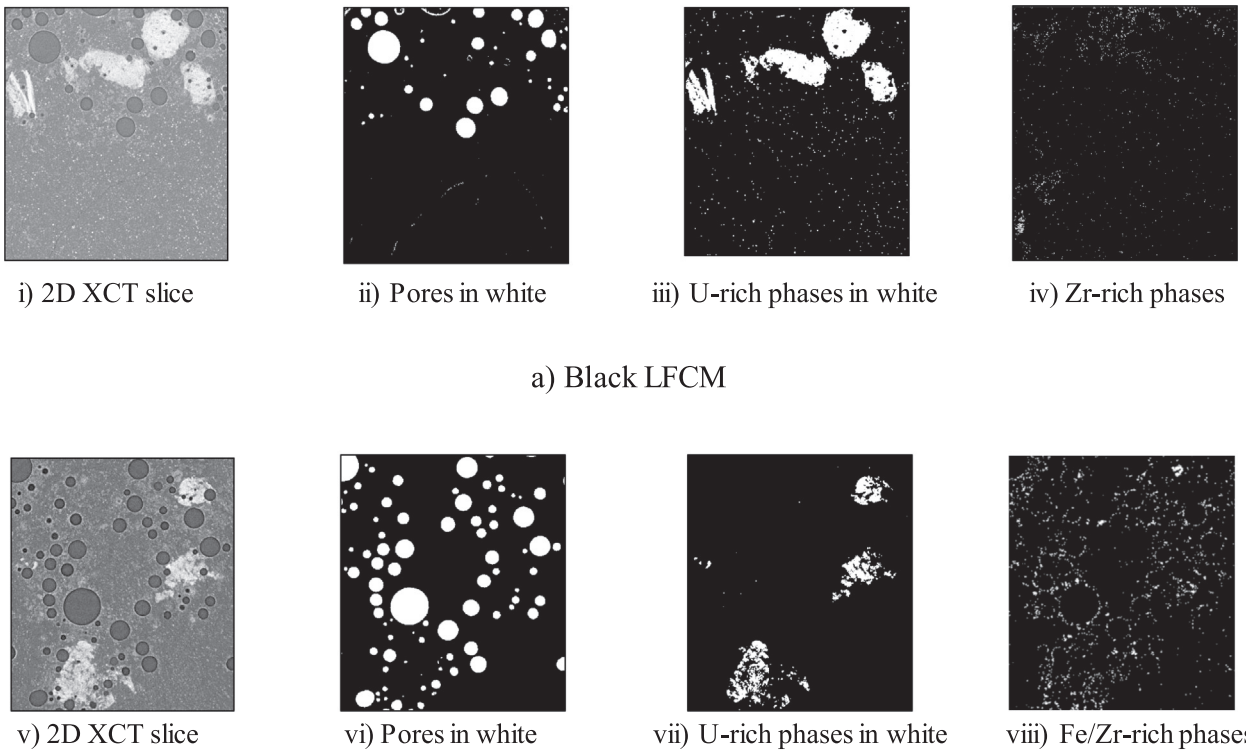

Fig. 4. XCT screenshots illustrating the segmented phases for a) black LFCM: i) 2D XCT slice, ii) pores, iii) U-rich, iv) Zr-rich; and b) brown LFCM: v) 2D XCT slice, vi) pores, vii) U-rich, viii) Fe/Zr-rich.

investigated volumes. The width of the crack in the black LFCM sample was considerably larger than in the brown LFCM.

Segmentation of the void volume, including cracks wherever applicable, was performed on all the cropped datasets, corresponding from zero load up to failure. No differences in total void volume were identified between tomograms as load increased, except for the last scan where in both cases (black LFCM; brown LFCM) wide cracks generated due to excessive loading. This behaviour implies that both materials

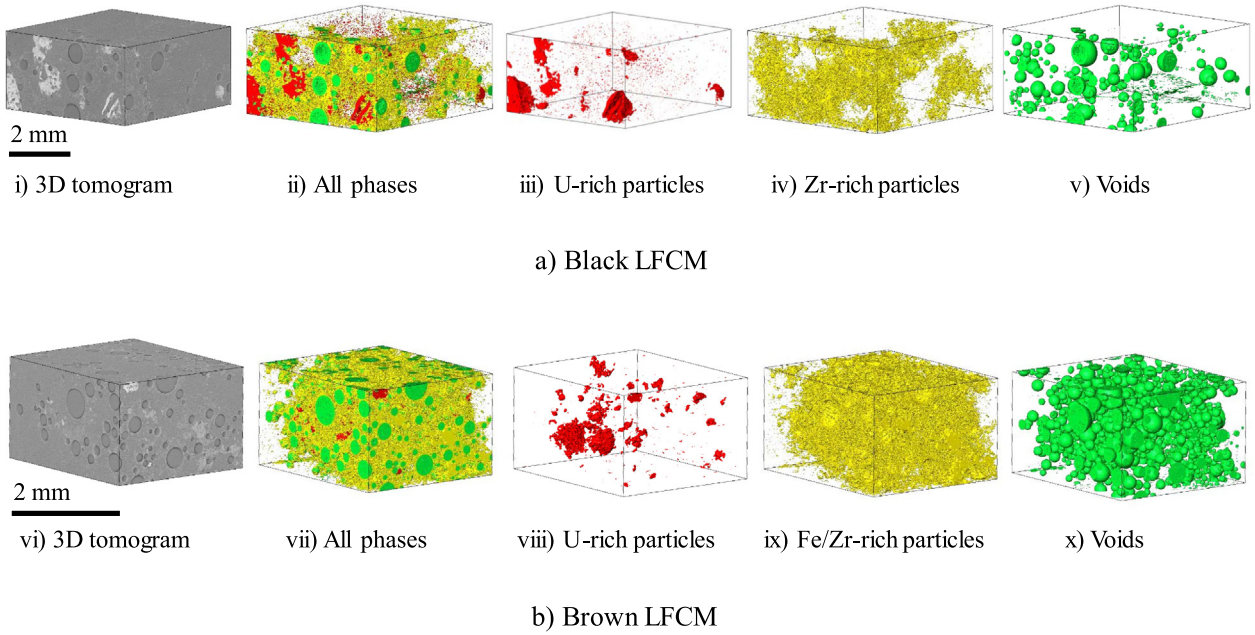

Fig. 5. 3D cuboids illustrating the segmented phases for a) black LFCM: i) 3D tomogram, ii) all phases, iii) U-rich, iv) Zr-rich, v) voids; b) brown LFCM: vi) 3D tomogram, vii) all phases, viii) U-rich, ix) Fe/Zr-rich, x) voids.

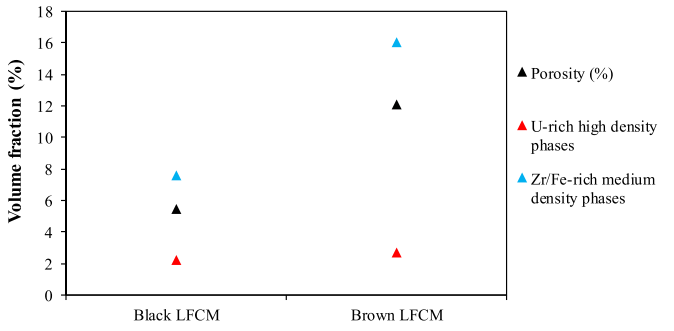

Fig. 6. Volume fractions of different phases present in the two sample materials tested on the DLS I12 beamline. Results were segmented from the pre-loaded datasets.

exhibit a similar type of brittle failure, with no signs of micro-cracking, which would reflect an increase in the total void volume, in the proximity of peak load. The above hypothesis is also corroborated from the load paths of both samples, and especially black LFCM which failed during topping up the load (Fig. 9). The immediate drop of load beyond the peak value is typical for brittle materials.

The correlation between phase volume fractions and failure load for the two samples investigated are shown in Fig. 10. As expected, sample failure occurs at a lower load when the sample contains greater porosity, and the same trend can be observed for the U-rich and Fe/Zr-rich phase volume fractions. Pore size distribution analysis, performed by combining the "Material Statistics" and "Label Analysis" Avizo modules [23], generated the histogram shown in Fig. 11. Both samples exhibited almost the same total pore volume in the "small pores regime" (0 mm^3

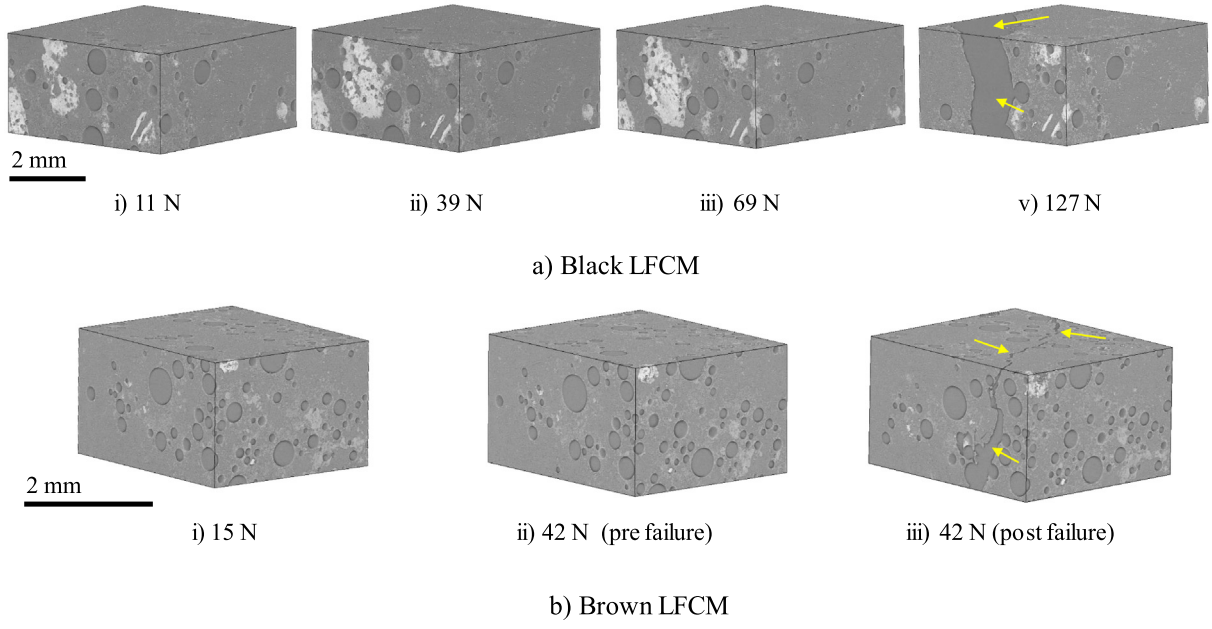

Fig. 7. Evolution of structural degradation as load increases for the two sample materials tested on the DLS I12 beamline. Yellow arrows point at cracks formed during loading.

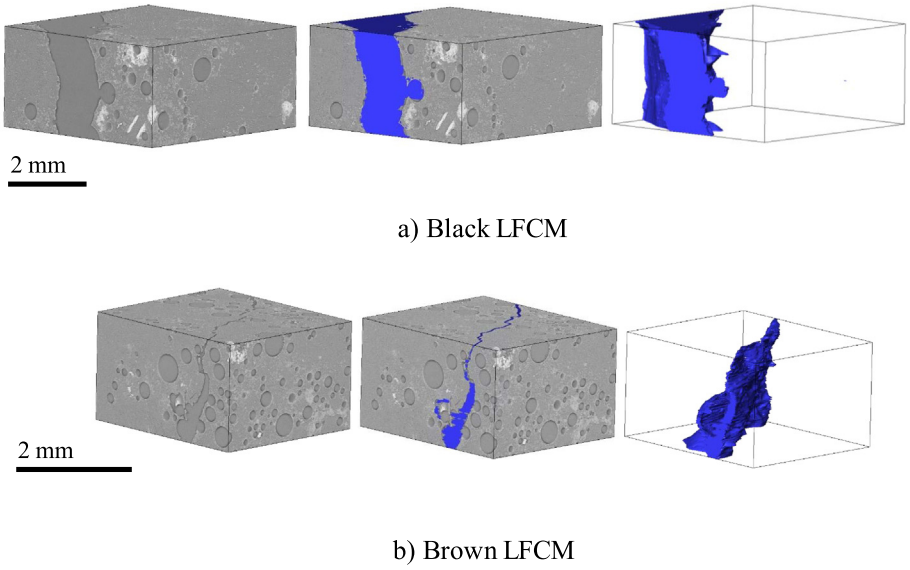

Fig. 8. 3D cuboids illustrating segmented crack volume network developed after sample failure.

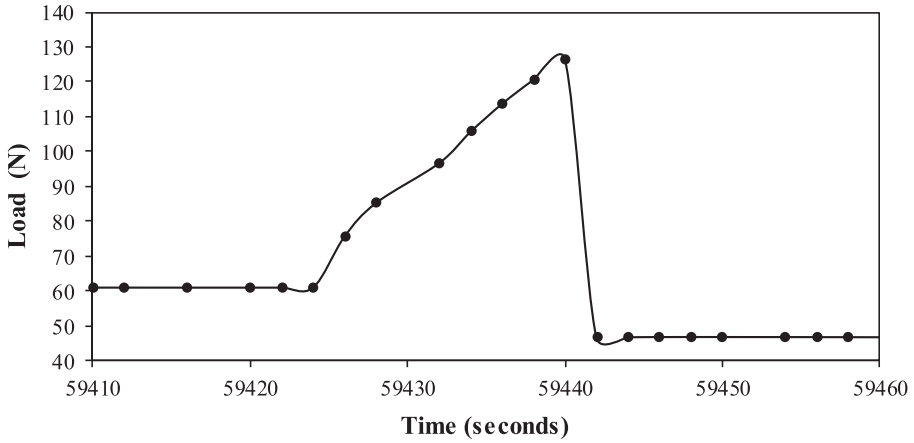

Fig. 9. Load path recorded for black LFCM sample during the last loading cycle where failure occurred.

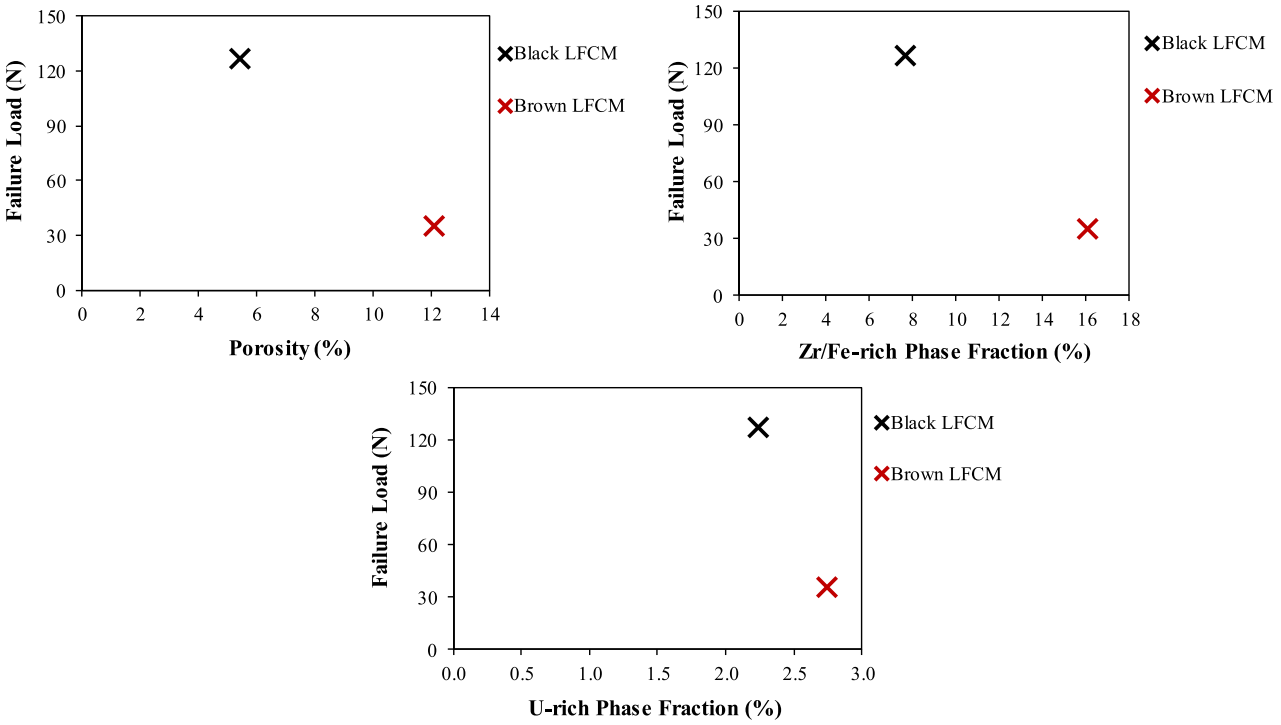

Fig. 10. Correlation between failure load and fraction volumes for the two sample materials tested on the DLS I12 beamline: a) pores; b) Fe/Zr-rich phases; c) U-rich phases.

to 0.001 $mm^{3)}$. It can be observed that the brown LFCM sample contained more pores of intermediate size (0.001 mm^3 to 0.1 mm^3) than did the black LFCM. The corresponding difference is more significant when comparing the number of large pores (0.1 mm^3 to >10 mm^3) present in the investigated volumes. This greater number of individual large pores present within the brown LFCM sample explains why its total porosity is almost double that of the black LFCM (Fig. 6).

3.3. Digital volume correlation

To extract the displacement and strain fields at the different loading stages, the deformed volume images were successively compared against the reference volume image set-up as the latter was determined for every sample. The Avizo "XDigital Volume Correlation" extension module [23] was employed to quantify the loading-induced

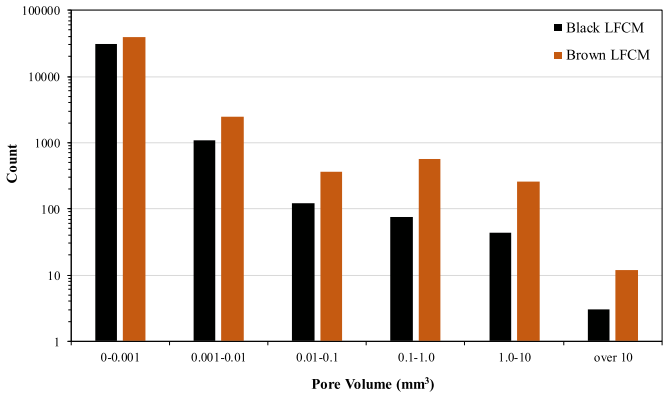

Fig. 11. Pore size distribution for the two sample materials investigated on the DLS I12 beamline performed using Avizo image segmentation modules.

deformation on the samples tested. The original tomograms were processed as follows to reduce computational time and be compatible with software recommendations. Open source software ImageJ [24] was used to convert the original 32-bit images to 8-bit images. Image noise reduction was performed by using the despeckle median and smooth filters [24]. Data-cropping was essential not only to reduce the computational cost but also to produce ideal geometric volumes. The sizes of the cropped datasets for black LFCM and brown LFCM samples that were used specifically for DVC analysis were 1452 voxel × 1050 voxel × 621 voxel (4.61 mm × 3.32 mm × 2.03 mm) and 1240 voxel × 1126 voxel × 413 voxel (4 mm × 3.66 mm × 1.33 mm), respectively. Comparisons between the DVC volumes used and the corresponding entire material volumes for both black and brown LFCM samples are shown in Figs. 12 and 13. The samples were not perfect cuboids; therefore, the relevant dimensions given closely approach reality.

The Avizo "XDigital Volume Correlation" extension module is based on a double mechanism to determine the deformation occurring between two relevant image stacks. A subset-based (local) approach is initially employed to capture the large displacements within the probed sample volume. Therefore, a coarse grid is primarily implemented. The large displacement field, as calculated via the local approach, is subsequently used as input to initialise a more robust finite element (FE)-based (global) DVC algorithm. The corresponding global-approach mesh is significantly finer, allowing displacement field calculations of greater precision.

The 3D tomograms related to the scans conducted after the sample failure were not considered for analysis. The significant width of the cracks formed during the last loading cycle would generate unreliable and erroneous displacement and strain fields [25]. The scans performed at the first loading cycle for each sample were adopted as the initial reference volumes. This approach was based on the considerable sample movement and rotation occurred after immediate contact with the indenter. As a result, erroneous results were produced when the corresponding DVC analysis was performed for the transition from zero load to the first loading cycle. After applying the initial small load, the sample was more stable and the transition to higher loads provided

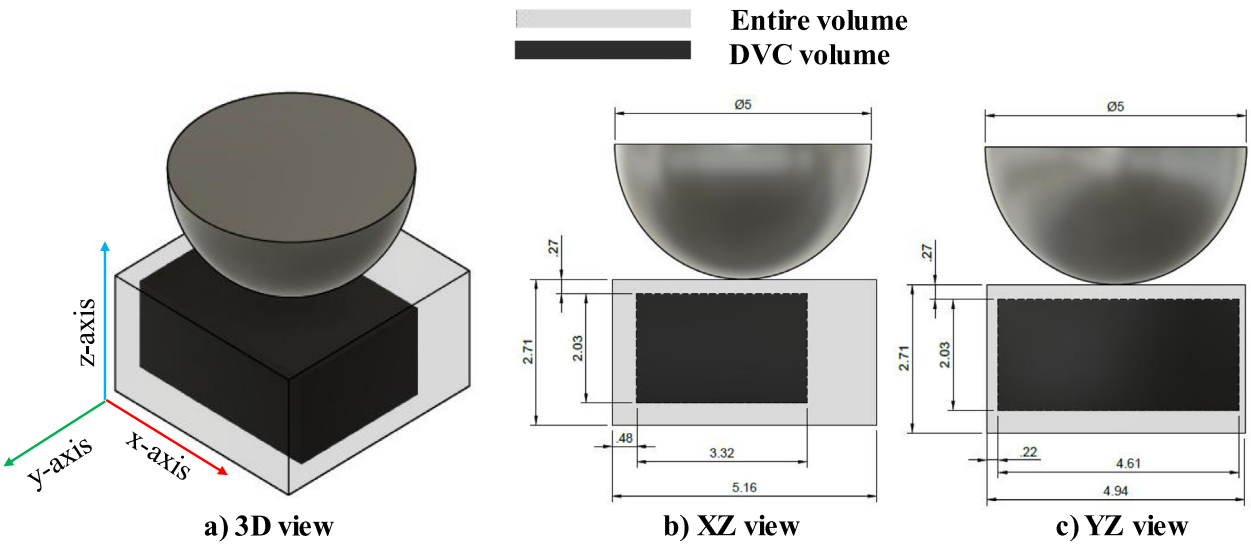

Fig. 12. Schematic of entire material and relevant DVC volume adopted to investigate mechanical properties of the black LFCM sample: a) 3D view; b) planar xz view; c) planar yz view. All dimensions are given in mm.

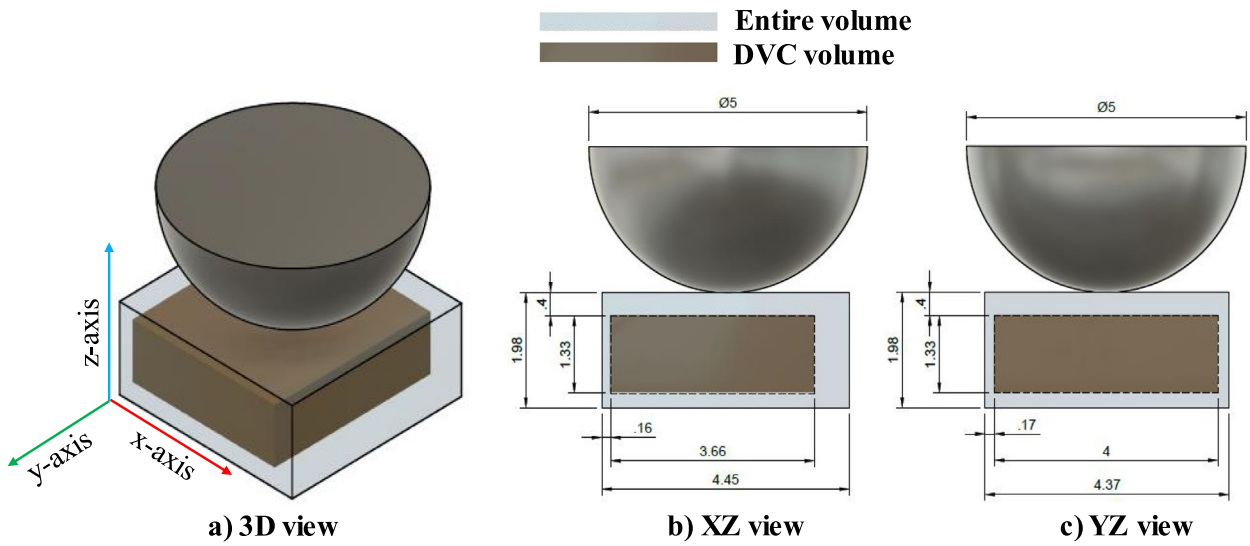

Fig. 13. Schematic of entire material and relevant DVC volume adopted to investigate the mechanical properties of the brown LFCM sample: a) 3D view; b) planar xz view; c) planar yz view. All dimensions are given in mm.

Table 3
Test strain values imposed on the cuboids used for DVC to evaluate reliability of the method.

Sample material	ε_{xx}	ε_{yy}	ε_{zz}
Black LFCM	0.010	0.010	0.020
Brown LFCM	0.011	0.010	0.020

more reliable results for comparison. The concept of using scans associated with small initial loading as the reference data for DVC analysis has been commonly followed in the literature [14].

Prior to performing DVC on the real data, a virtual displacement method was employed to test the reliability of the image registration technique, which is used to correlate the different image datasets. On all occasions, the reference tomogram (corresponding to the first loading cycle) was subjected to certain prescribed displacements across the three axes. The test strain values imposed across the three axes to evaluate the reliability of the method are shown in Table 3 for both samples. The reference and deformed volumes were then analysed to evaluate if the DVC outputs (displacement; strain field) were close to the initial, pre-defined deformation values.

Metric and transform ports were set to "correlation" and "translation and rotation" modes, respectively [23]. Correlation threshold was set to 0.5. After running the local approach, a displacement field and a strain tensor were created along with a metric map. The displacement field was subsequently passed as an input file to run the global algorithm. Maximum number of algorithm solver iterations was set to 30 while the convergence criterion was maintained steady at 0.001 for all analyses. Various sizes of the FE mesh implemented were tested in the form of a sensitivity analysis to determine which mesh best described the pre-defined deformation state. The ideal sub-volume sizes (as determined from the local approach) and mesh sizes (as determined from the global approach) were used as input DVC parameters for analysis of the real XCT data corresponding to successive loads. The results of the sensitivity analysis performed based on the virtual displacement concept using the local DVC approach are shown in Figs. 14–15. The dotted red lines demonstrate the expected strain values after the virtual displacement was imposed. The coefficient (Figs. 14a, 15a) demonstrates the quality of the correlation. This is a metric indicator to reveal the best mapping of the corresponding subset in the reference volume with equivalent subsets in a subsequent volume. The quality of the correlation improves while approaching unity. Figs. 14b and 15b demonstrate the axial strain values determined after performing the virtual displacements on the reference image volumes. Points which are closer to the dotted lines demonstrate enhanced correlation for the corresponding sub-volume size.

A similar process was followed for the relevant FE-based (global) models. The results showed considerable consistency. The sub-volume size for the local approach and the mesh cell size for the global approach, as selected for the analyses of both samples (black LFCM; brown LFCM) are summarised in Table 4.

The reference and deformed volume datasets, which were used in pairs to monitor the sample internal deformation as load increased are given in Table 5 along with the correlation coefficient of the DVC runs. The corresponding sizes of all the final FE-based tetrahedral meshes

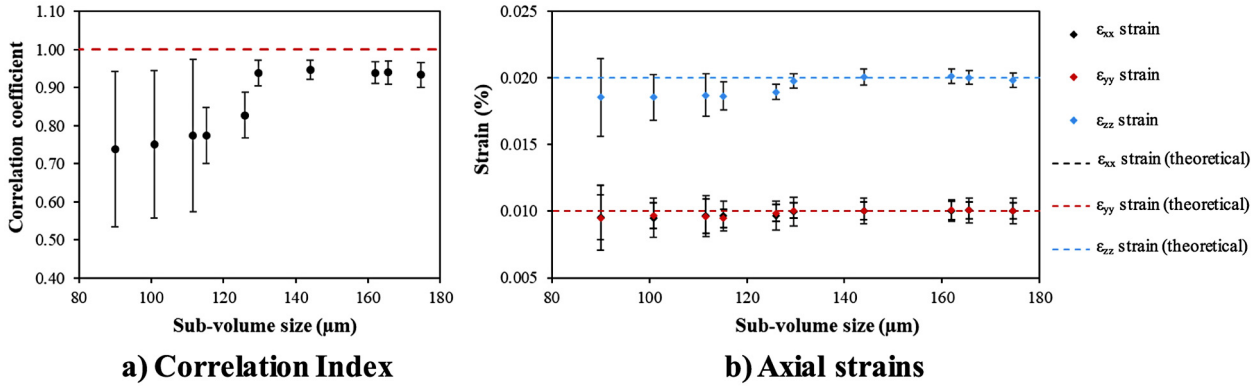

Fig. 14. Sensitivity analysis results illustrating the effect of sub-volume size on: a) correlation coefficient; b) axial strains for the black LFCM sample. Dotted lines represent expected strain values after the virtual displacement was imposed.

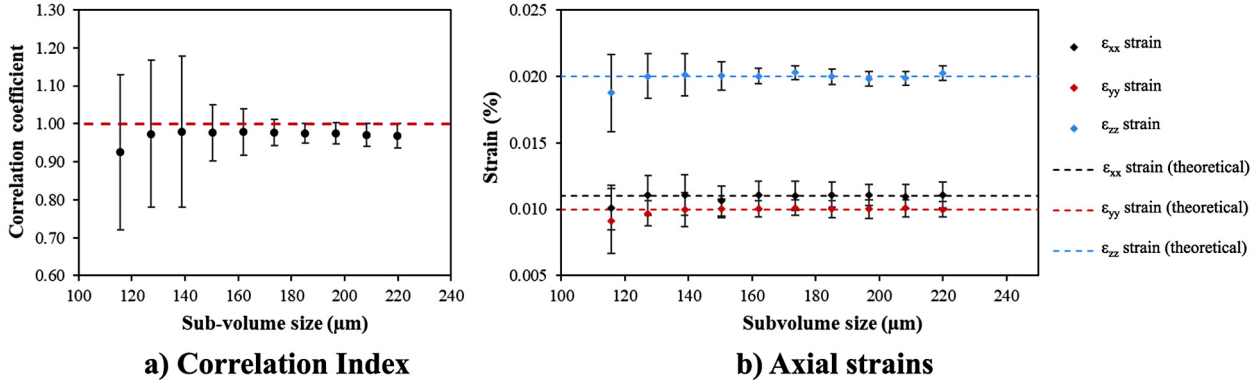

Fig. 15. Sensitivity analysis results illustrating the effect of sub-volume size on: a) correlation coefficient; b) axial strains for the brown LFCM sample. Dotted lines represent expected strain values after virtual displacement was imposed.

Table 4
Values of sub-volume and mesh cell sizes selected to perform DVC analysis on the XCT data collected for the two sample materials tested on the DLS I12 beamline.

Sample material	Sub-volume size - Local (μm)	Mesh cell size - Global (μm)
Black LFCM	130	90
Brown LFCM	174	116

Table 5
Data combinations used to apply the DVC analysis for the two sample materials tested on the DLS I12 beamline.

DVC trial number	Reference dataset (as per load)	Deformed dataset (as per load)	Number of nodes	Correlation coefficient
Black LFCM				
1	11 N	39 N	7608	0.955
2	11 N	69 N	7608	0.953
Brown LFCM				
1	15 N	42 N	4756	0.976

implemented are also included. The results of the DVC analysis provided quantitative information about the deformation occurred within the investigated sample volumes. More specifically, displacements at every node of the implemented model as well as strains at each element of the generated mesh were extracted on all occasions across the three axes. In total, nine 3D visualised datasets were created per DVC run, including three displacement maps (u_x, u_y and u_z, reflecting the nodal displacements across the x, y and z axes, respectively), three axial strain maps/tensors (ε_{xx}; ε_{yy}; ε_{zz}) and three shear strain maps/tensors (ε_{xy}; ε_{xz}; ε_{yz}).

The relevant 3D displacement and strain maps for the black LFCM sample are illustrated in Figs. 16–18. Displacement and strain maps generated after correlating the data produced during the first two loading cycles (transition from 11 N to 39 N) exhibited uniform behaviour. However, changes in the sample microstructure are anticipated to have occurred during the load increase to 69 N, as shown in the respective DVC maps. Displacements measured across the three axes (u_x; u_y; u_z) strongly diverged. Axial and shear strain maps revealed a zone of elevated values at the same corner location, implying that load-induced discontinuities had developed within the sample volume.

A similar process was followed to investigate the behaviour of the brown LFCM sample. Only a single pair of datasets was analysed (15 N to 42 N), since sample failure occurred under a minimal load. The relevant results including displacement and strain maps are shown in Figs. 19–21.

Even though only the transition from the first to the second loading cycle was analysed using DVC, certain remarks can be made. The black LFCM sample did not exhibit any significant variations in displacement and strain values during the same period (from the first to the second loading cycle). However, a slightly different behaviour was observed for the brown LFCM. The displacement profile (Fig. 19) reveals strongly non-uniform deformation across the top surface of the analysed volume. The diagonal stripe of larger u_z values shown in Fig. 19c seems to be in good agreement with the localised increased axial strains noted predominantly across the y–axis (ε_{yy} in Fig. 20b) and, to a lesser extent, across the z–axis (ε_{zz} in Fig. 20c). With regards to the displacements reported in the legends of Figs. 16 and 19, it is important to note that the relevant values are given in μm.

3.4. Mechanical properties

The DVC process enabled quantitative analysis, in addition to the qualitative comparison described in the previous section. The displacement and strain data, as extracted for all the nodes and elements of the 3D meshes implemented, were used as inputs to examine the prospect of determining the mechanical properties of the materials tested. Alternative approaches were employed to estimate Young's modulus and Poisson's ratio values. The first method was based on the displacement data.

Fig. 22 provides an illustrative explanation of the concept adopted to determine the Young's modulus, following this method. DVC analyses enabled determining the vertical displacements in all the relevant volume nodes. The vertical displacements of all the nodes belonging to

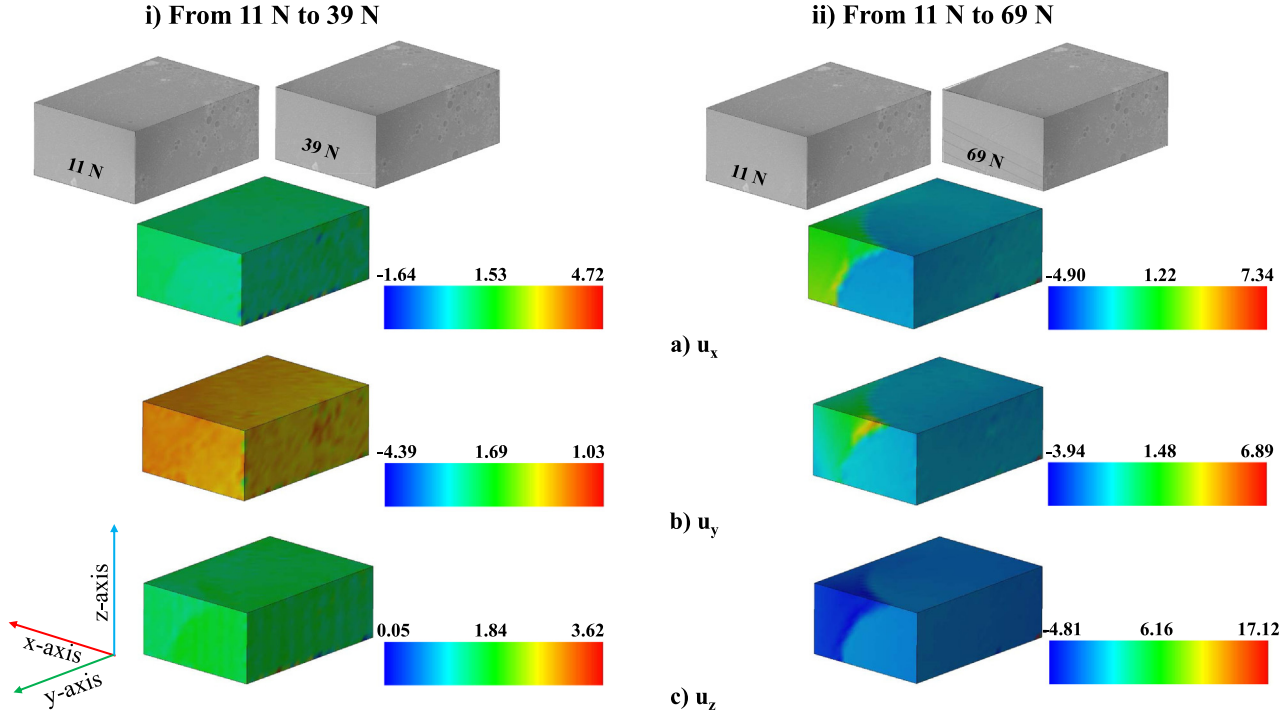

Fig. 16. DVC-measured displacement fields (u_x; u_y; u_z) in the stepwise indentation loading test performed on the black LFCM sample. Dimensions are given in μm.

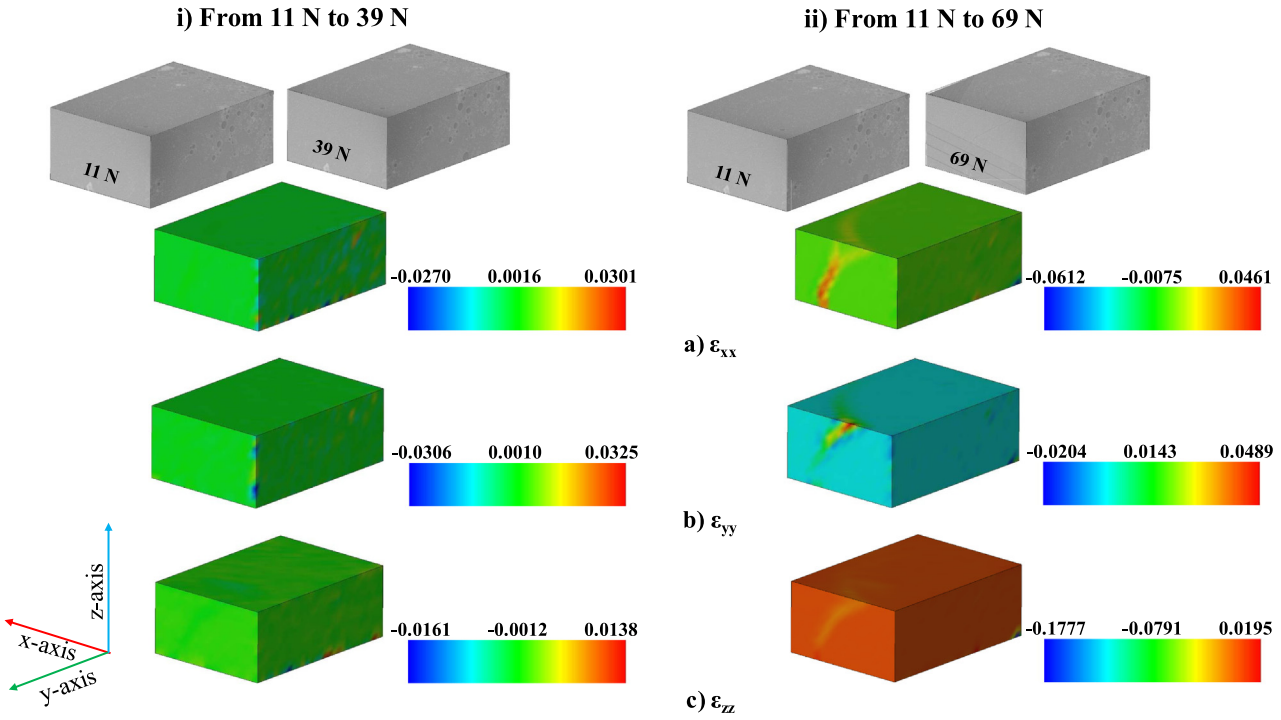

Fig. 17. DVC-measured axial strain fields (ε_{xx}; ε_{yy}; ε_{zz}) in the stepwise indentation loading test performed on the black LFCM sample.

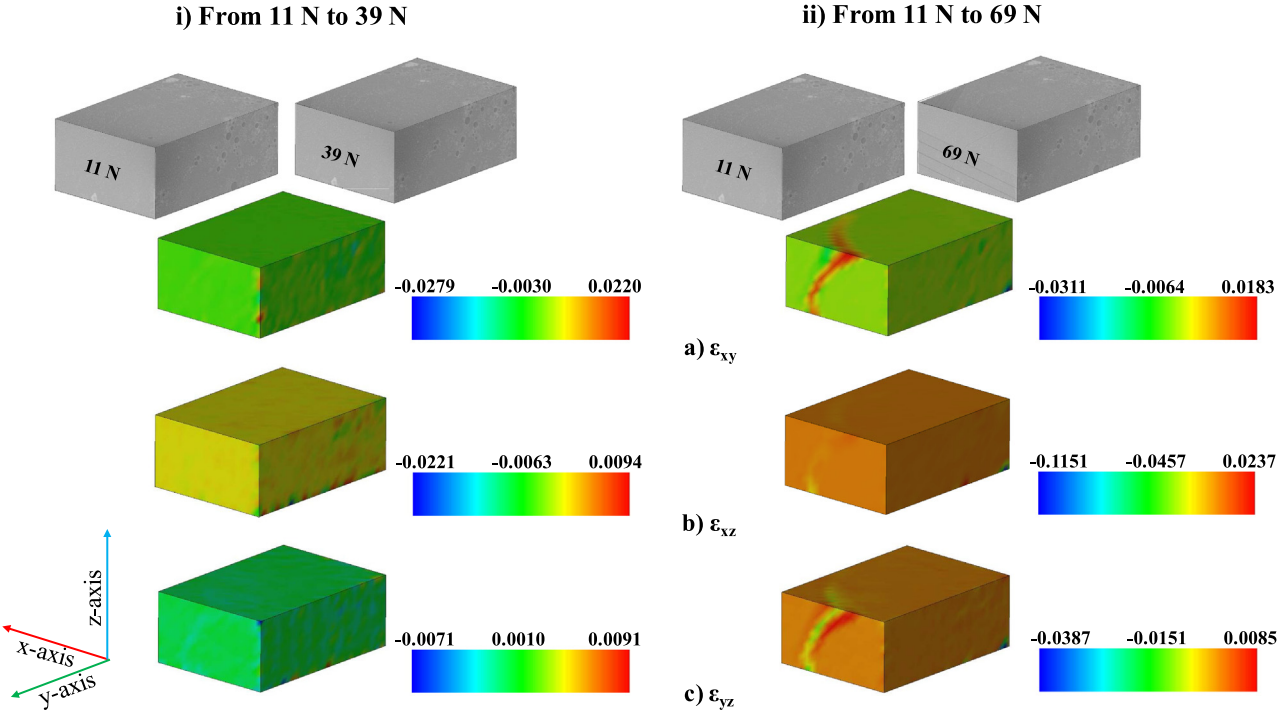

Fig. 18. DVC-measured shear strain fields (ε_{xy}; ε_{xz}; ε_{yz}) in the stepwise indentation loading test performed on the black LFCM sample.

the top surface of a DVC cuboid were averaged. Thus, the average vertical displacement of the top surface, denoted as U_1 on Fig. 22, was calculated. The same process was followed to determine the average vertical displacement of the bottom surface, denoted as U_2. The vertical strain ε_{zz}, occurring during a load transition phase is based on Eq. 1, where L_0 is the initial sample height and L_1 is the sample height after loading.

$$\varepsilon_{zz} = \frac{L_1 - L_0}{L_0} \tag{1}$$

Based on the schematic shown in Fig. 22, the sample deformation can also be calculated based on Eq. 2.

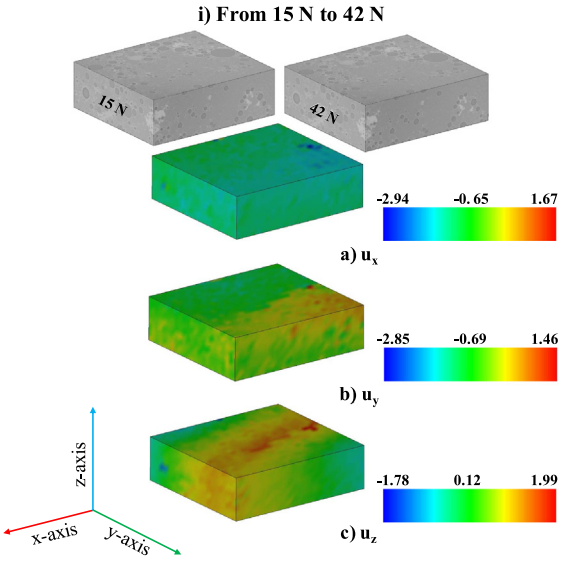

Fig. 19. DVC-measured displacement fields (u_x; u_y; u_z) in the stepwise indentation loading test performed on the brown LFCM sample. Dimensions are given in μm.

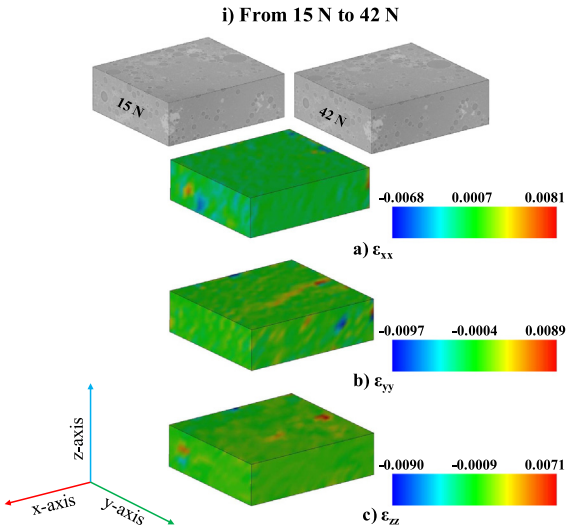

Fig. 20. DVC-measured axial strain fields (ε_{xx}; ε_{yy}; ε_{zz}) in the stepwise indentation loading test performed on the brown LFCM sample.

$$L_1 - L_0 = U_2 - U_1 \tag{2}$$

Combining the Eqs. 1 and 2 enables determining the vertical strain ε_{zz} based on the average displacements U_1 and U_2, as determined via the DVC analysis, and the sample initial height (Eq. 3).

$$\varepsilon_{zz} = \frac{U_2 - U_1}{L_0} \tag{3}$$

The above process was followed to determine the vertical strain ε_{zz} at all the load-transition phases. A similar workflow process to estimate the mechanical properties of quasi-brittle, heterogeneous materials has been available in the literature [16]. Based on the vertical strain ε_{zz} values determined at each loading step, Young's modulus was

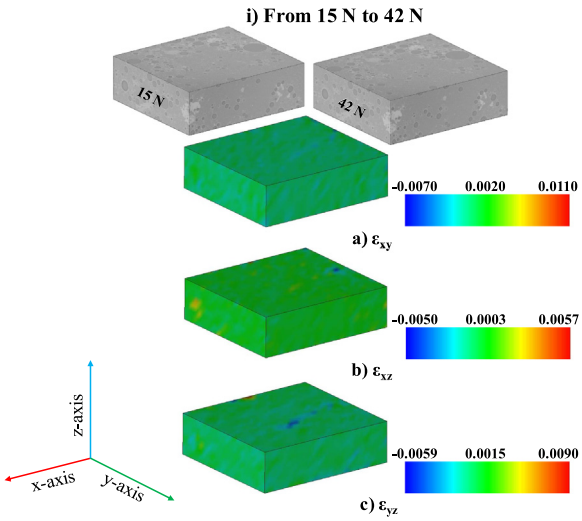

Fig. 21. DVC-measured shear strain fields (ε_{xy}; ε_{xz}; ε_{yz}) in the stepwise indentation loading test performed on the brown LFCM sample.

subsequently calculated based on Hook's law according to the following equation:

$$E = \frac{\sigma_{zz}^{*}}{\varepsilon_{zz}} = \frac{\Delta F}{A \cdot \varepsilon_{zz}} \tag{4}$$

Where E is the Young's modulus (measured in MPa), σ_{zz}^{*} is the stress equivalent of a uniaxial compression state, ΔF is the difference in load between two successive loading stages (measured in N) and A is the sample surface (measured in mm^2). The above formula has been adopted as a simplification of the stress state developed in the sample volumes during loading. Hertzian indentation does not generate a uniform stress state (e.g. uniaxial tension/compression), and therefore, Eq. 4 may not be appropriate for use. However, the sample volumes were significantly limited and cannot be considered as infinite plates, as in a classical indentation problem. In addition, the strain profiles measured by DVC analysis showed a relatively uniform vertical axial strain distribution during the early loading stages, resembling a uniaxial compression behaviour. Since the Poisson ratio was unknown and its value could not be predicted due to sample heterogeneity, and load–penetration depth curve during unloading was not available, analytical related to indentation loading expressions could not be used to determine the Young's modulus. Therefore, our method, even though a simplification, was considered to provide at least quantitatively, a way of comparing the values of Poisson ratio and Young's modulus between different types of simulants.

A specific Young's modulus value was calculated for every separate load combination and, consequently, DVC analysis performed per sample. In the case of black LFCM, where two different load transition scenarios were investigated using DVC, an average Young's modulus value was calculated. The corresponding results obtained after applying the displacement method are given in Table 6. To corroborate the results obtained from the displacement method and to monitor the uniformity of material stiffness within the entire investigated volume, similar calculations were made using the available vertical strain ε_{zz} data (Figs. 17c, 20c.

The average strain was determined on each occasion, considering the values exported from all the mesh elements. Subsequently, the Young's modulus was calculated using the Eq. 4. The results are provided in Table 7. A good agreement between the two methods can be observed.

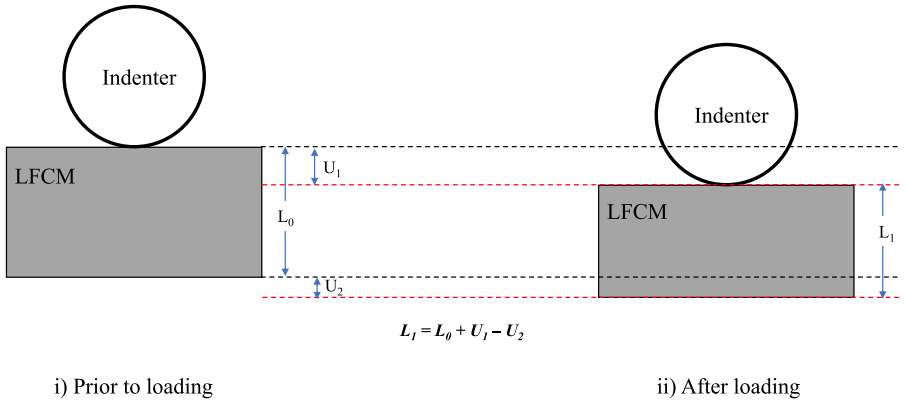

Fig. 22. Schematic representation of the method applied to calculate the vertical strain ε_{zz} based on the nodal displacements determined via DVC analysis.

Table 6
Young's modulus determined after applying the displacement method.

Sample material	Young's modulus (GPa)
Black LFCM	6.14 (±1.02)
Brown LFMC	16.26

Table 7
Young's modulus determined after applying the strain method.

Sample material	Young's modulus (GPa)
Black LFCM	5.80 (±0.93)
Brown LFMC	15.80

The relatively non-uniform vertical strain distributions, as shown in the relative DVC maps (Figs. 17c, 20c), could imply inconsistent material stiffnesses. Therefore, in addition to calculating the average strain values considering the entire investigated volumes, potential variations of the Young's modulus within the samples were also evaluated. The xy planar average vertical strains were determined across the heights of the DVC volumes generated. Subsequently, xy planar Young's moduli were estimated based on the relative compressive stresses (σ_{zz}^*).

The alteration of stiffness across the height of the inspected DVC volume per sample is illustrated in Fig. 23. Based on the axis configuration selected, high z values correspond to areas closer to the top of the sample. Scattering of the Young's modulus values across the sample height can be observed in both samples. Results from the black LFCM analysis revealed a trend of stiffness decay, while moving towards the sample top surface. The modulus values calculated based on the two available

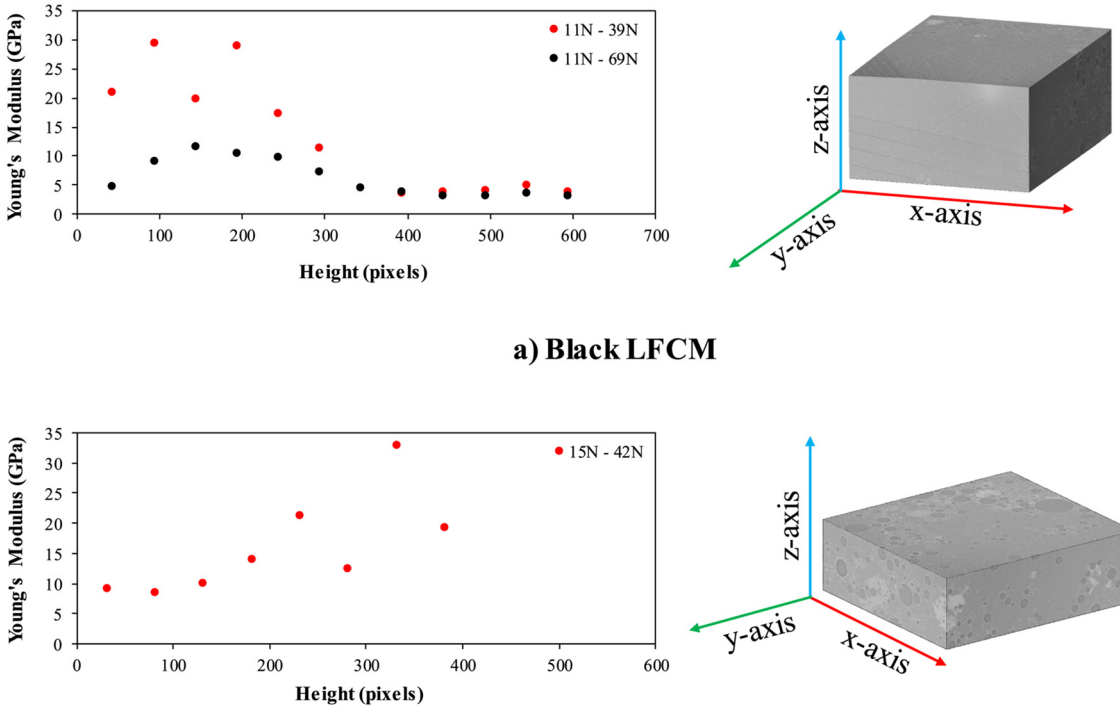

Fig. 23. Variation in stiffness (Young's modulus) across the height (z-axis) of the DVC volumes based on the average xy planar strain for the two sample materials tested on the DLS I12 beamline: a) black LFCM; b) brown LFCM.

Table 8
Poisson's ratio values calculated for the two sample materials tested on the DLS I12 beamline based on the average axial strains determined from the relevant DVC data.

Sample material	Poisson's ratio v_{xz}	Poisson's ratio v_{yz}
Black LFCM	0.64	0.36
Brown LFCM	0.42	2.42

sets of DVC data (11 N to 39 N, 11 N to 69 N) are in relatively good agreement. A trajectory to lower stiffness values until a plateau is reached can be noted while approaching closer to the sample top surface. The brown LFCM sample also exhibited a considerable variation of Young's modulus values across the sample height, though with an opposite trend compared to the black LFCM. From analysis of the acquired data sets, it is observed that the top section of the brown LFCM specimen was noticeably stiffer.

An equivalent approach was followed to estimate the Poisson's ratio for each sample. The method employed was based on the strain data collected. Lateral expansion across both x and y axes, both being perpendicular to the contraction direction (z-axis), was monitored to calculate separately the relevant Poisson's ratio values v_{xz} and v_{yz}. Average strains across all the axes (ε_{xx}; ε_{yy}; ε_{zz}) were determined, using the available DVC data, and considering the entire corresponding DVC-related investigated volumes. The relevant Poisson's ratios calculated using the theory of elasticity ($v_{xz} = -\varepsilon_{xx}/\varepsilon_{zz}$; $v_{yz} = -\varepsilon_{yy}/\varepsilon_{zz}$), for each sample are summarised in Table 8.

The calculations reveal large discrepancies between the Poisson's ratio values determined for different orientation planes. In compliance with the process followed for the Young's modulus, distribution of the Poisson's ratio across the height of the DVC volumes was performed for each sample tested on the DLS I12 beamline. Initially, average xy planar axial strains (ε_{xx}; ε_{yy}; ε_{zz}) were calculated for every characteristic z-axis (height) value. The DVC data corresponding to the primary loading cycles only were considered to ensure that the material behaviour remained linear elastic for the range of data being analysed. Based on this arrangement, the relevant distribution of Poisson's ratio (ν_{xz}) across the sample height was estimated. The results are given in Fig. 24. Noticeably, a significant variation in Poisson's ratio can be observed for all the samples tested.

3.5. Finite element modelling

The hypothesis of a uniaxial compression stress state, as expressed via Eq. 4, was necessary to provide numerical solutions of the problem discussed in this paper. However, potential effect of this simplification on the calculated Young's modulus value was also investigated. Finite element (FE) analyses were performed using the software package ABAQUS 6.14 [26] to simulate the indentation tests performed on the materials. The geometry of the samples and the indenter was accurately reproduced in the FE models implemented. The results of the FE analyses were used to reproduce the ratio shown in Eq. 4, which was adopted to derive the Young's modulus based on the DVC analyses. The Young's modulus test value, used as input for the FE analyses, was compared against the corresponding ratio of Eq. 4. Potential variation between the two values accounts for the effect of the uniaxial compression stress state hypothesis (instead of indentation) on the value of the material Young's modulus.

3.5.1. FE models

Two principal FE models were produced to simulate both black and brown LFCM indentation tests. The geometries adopted were identical to those described in Figs. 12 and 13. The cuboids created to simulate the "lava" samples were partitioned to enable visualisation of the corresponding DVC-associated interior volumes. Realistic representation of

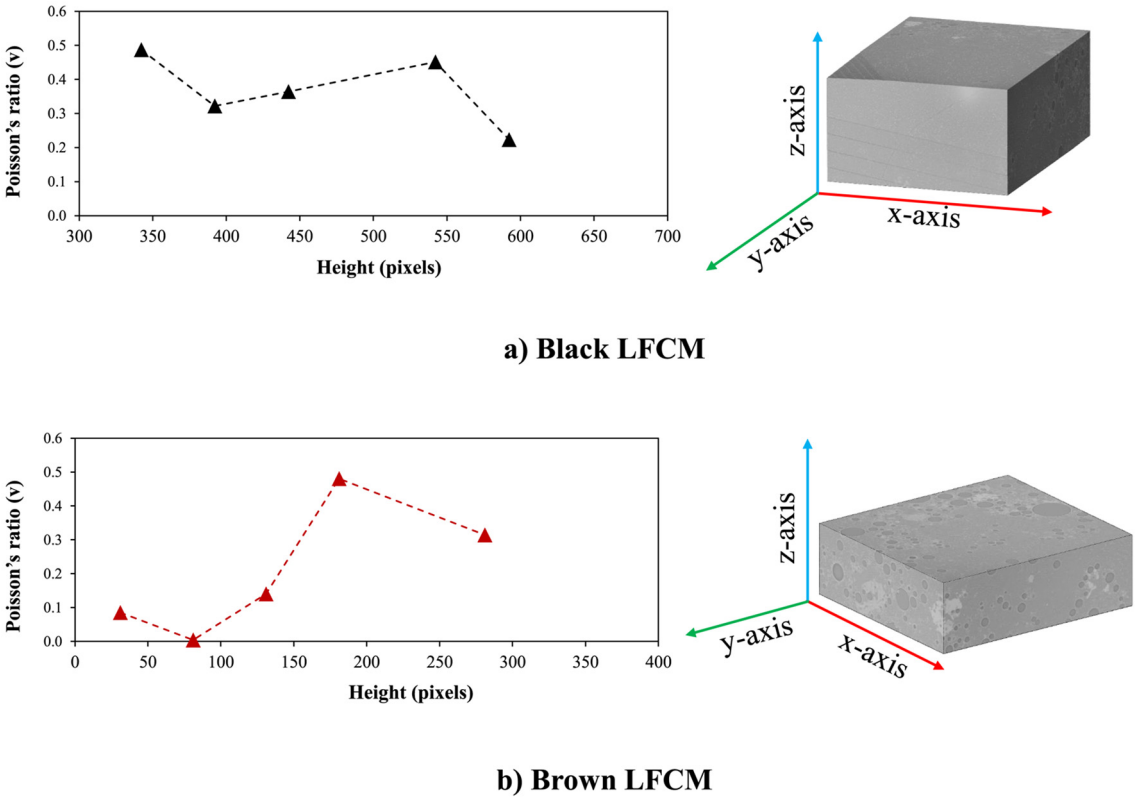

Fig. 24. Variation in Poisson's ratio (v) across the height (z-axis) of the DVC volumes based on the average xy planar strain for the two sample materials tested on the DLS I12 beamline: a) black LFCM; b) brown LFCM.

the sample microstructure was beyond the scopes of this FE modelling work package. Therefore, both samples were simulated as homogeneous solids.

3.5.2. FE type, mesh, and material modelling

Three-dimensional eight-node hexagonal solid elements (C3D8) with hourglass control and reduced integration were used to build the meshes of the "lava" samples. The indenter was modelled as a 3D discrete rigid body. Mesh convergence studies were conducted to determine the optimum element size, providing an accurate solution combined with minimum computational time. Therefore, the approximate global element size for both meshes was 0.3 mm. Since the investigation of the sample failure state was not part of the FE modelling work, both "lava" materials and the ZrO_2 Hertzian indenter were modelled as isotropic, elastic materials. The Young's modulus and Poisson ratio for ZrO_2 were set equal to 210 GPa and 0.22, respectively. Since the material properties of elasticity for both black and brown LFCM were unknown, theoretical values were adopted to implement the FE analyses. Therefore, test values of 6 GPa and 0.3 were used as input data for the Young's modulus and Poisson ratio of both materials.

3.5.3. Boundary conditions, interaction properties and load application

The bottom surface of the black and brown LFCM volumes was fixed against all translation and rotation degrees of freedom. A reference point was created at the top of the indenter combined with a body constraint, ensuring rigid body movement of the indenter. The reference point was fixed against rotation and movement across all directions except for vertical displacement (across z-axis). Surface-to-surface contact was selected to simulate the interaction properties between the indenter and the samples. A contact surface pair comprised of the outer surface of the indenter and the top surface of the "lava" volumes was defined. The normal behaviour of the system was modelled with a hard contact pressure-overclosure relationship, allowing surface separation under tension, and restricting node penetration under compression. A penalty contact algorithm with a friction coefficient equal to 0.5 was employed to describe the tangential behaviour of the contact properties. A displacement-controlled method was selected to simulate the loading process. Therefore, a prescribed vertical displacement of 0.5 mm was implemented at the reference point, ensuring the indenter moves as a rigid body only across the z-axis.

3.5.4. FE results

Processing of the FE modelling results followed the methodology employed to analyse the DVC data (strain method). The first step of the analysis included calculating the average vertical axial strain ε_{zz} at each xy plane of the generated mesh. Consequently, planar average strain values were determined across the z-axis. These strain values were subsequently averaged to determine the total average ε_{zz} strain, in compliance with the process followed for the DVC analysis. This workflow was repeated for every increment of the analysis. The goal of the FE modelling work was to reproduce the ratio given in Eq. 4. Therefore, the hypothetical vertical stress σ_{zz}^* was determined, assuming uniaxial compression conditions, as explained in the Section 3.4. The following formula was employed at each increment of the analysis:

$$\sigma_{zz}^{*} = \frac{RF}{A} \tag{5}$$

where RF is the reaction force (N) applied at the reference point, and A is the surface area (mm^2) of the "lava" samples. Average vertical stress σ_{zz} at the top ($\sigma_{zz\text{-top}}$) and the bottom ($\sigma_{zz\text{-bottom}}$) surface of the samples as well as average Von Mises stress (σ_{VM}) were also calculated for the sake of comparison. The evolution of all stresses with loading is given in Fig. 25 for both black LFCM (a) and brown LFCM (b) samples. Screenshots of the vertical displacement contours profile at the end of the FE analyses are also illustrated. Comparison between the stress paths shown in Fig. 25 demonstrates that calculation of the hypothetical vertical stress σ_{zz}^* underestimates the stress levels generated on both samples as the indenter's-imposed load increased.

The ratio shown in Eq. 4, which was implemented to indirectly determine the value of Young's modulus based on the DVC data, was necessary to be reproduced based on the FE analyses performed. Therefore, calculation of the corresponding total average strain ε_{zz} and the hypothetical vertical stress σ_{zz}^* (Eq. 5) were combined. This ratio value was produced at every increment of the analysis and was subsequently compared against the Young's modulus adopted as a test input value to run the FE analyses.

Thus, the numerical correlation between the FE-based calculated ratio of Eq. 4 and the corresponding test input value of Young's modulus was produced to account for the effect of adopting uniaxial compression conditions instead of spherical indentation to solve the problem. Based on this correlation, revised values of Young's modulus could be recommended for both "lava" materials. The comparison between the hypothetical Young's modulus (E_{hyp}), as calculated by applying Eq. 4 on the relevant FE results, and the test input value adopted (E_{real}) is shown in Fig. 26. The average value of E_{hyp}/E_{real} ratio for the black LFCM sample is equal to 0.78 ($\pm$0.0037). The corresponding ratio for the brown LFCM sample is 0.67 ($\pm$0.015). These ratios were applied to the Young's moduli determined via the DVC analysis (shown in Table 7) to estimate the corrected stiffness of the "lava" materials. The corrected Young's moduli for the black LFCM and the brown LFCM samples are equal to 7.4 MPa ($\pm$1.19) and 23.5 GPa, respectively.

4. Discussion

Performing indentation loading with successive XCT and DVC on the samples tested on a synchrotron beamline is an effective method to determine the mechanical behaviour and the microstructure of materials. The radioactive nature of our samples hindered the possibility to use standard methods of mechanical testing (e.g. use of strain gauges), since a greater material volume would be required. The tomograms revealed the multiphase nature of the materials and the in-situ indentation their near brittle fracture behaviour.

Assuming that these surrogate, laboratory-manufactured materials behave similarly to the real Chernobyl LFCM inventory, a very rigorous decommissioning process needs to be followed to tackle their limited mechanical performance. The XCT scans performed to investigate the material microstructure revealed a considerable number of large pores for both our lab-manufactured black and brown LFCM-simulant samples. This extensive and diverse pore network has probably dominated the sample mechanical performance, affecting both their stiffness and load bearing capacities. Comparison between black and brown LFCM performance is challenging since their yielding mechanisms differ. The brown LFCM sample failed during the scanning process at a primary load, while the black LFCM crushed during topping-up of the load.

The limited amount of data collected based on the beamtime restrictions hindered the possibility to study in detail the failure mechanisms. Scans performed at considerably more load steps, especially close to failure loads, would enable a more in depth understanding of the failure process if combined with finer resolution. In such a scenario, crack initiation could be detected and linked with the microstructure. Tomograms associated with pre-failure loading did not exhibit any indication of weak zones related to potential failure. Both samples revealed a single macrocrack having formed across the thickness after failure. A wide, almost completely vertical crack was observed in the black LFCM sample (Fig. 8a), resembling a typical splitting-type failure analogous to a beam failure under flexural tension. It is interesting to note that the through thickness volume beneath indentation was relatively homogenous exhibiting a significantly limited number of pores. In contrast to black LFMC sample, a diagonal narrow crack is observed in the brown LFCM failure scan. However, such behaviour is not associated with a different failure mechanism (e.g. shear failure) but with the extensive pore

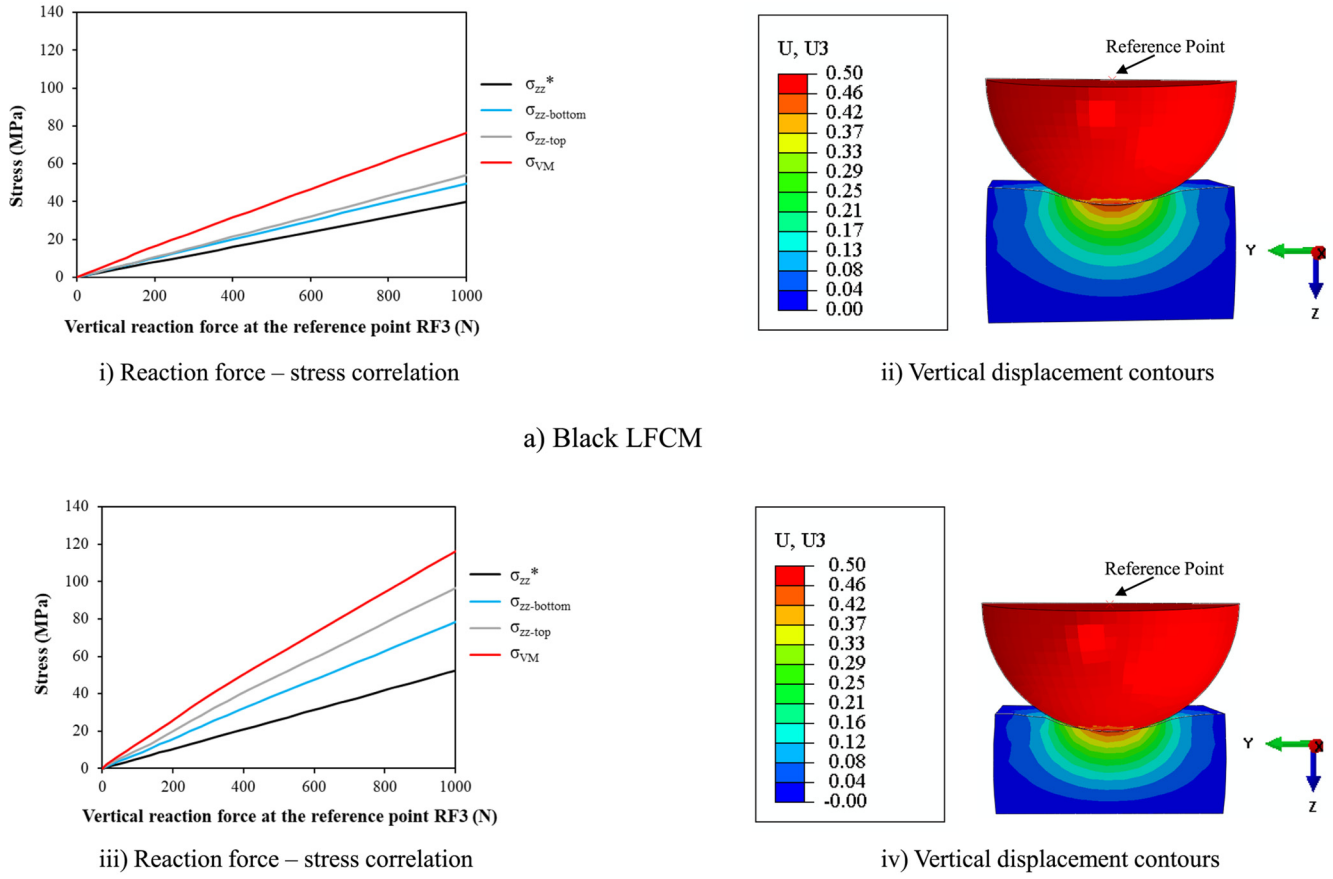

Fig. 25. Evolution of different stresses with loading for the black LFCM (ai) and the brown LFCM (biii) samples as determined via the corresponding FE analyses. Screenshots illustrating the profile of vertical displacement at the end of the analyses are also given for the black LFCM (aii) and the brown LFCM (biv) samples, respectively.

network lying beneath the indented area, which dominated the crack propagation pattern.

Based on the phase volume analysis (Fig. 6) and the pore size distribution histogram (Fig. 11), it was expected that brown LFCM would prove to be more brittle than black LFCM, since it revealed higher total porosity, greater number of large pores and lower calcium aluminosilicate glass phase volume.

It could be contradictive that DVC quantitative analysis showed the Young's modulus of brown LFCM to be almost 2.5 times greater than that of black LFCM, even if it was considerably more porous. Analytical

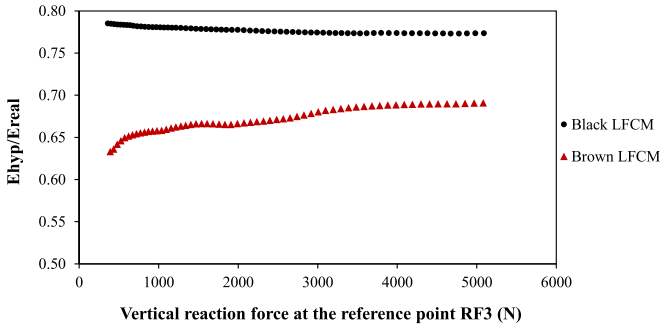

Fig. 26. Evolution of the ratio E_{hyp}/E_{real} with increased loading for both black and brown LFCM samples. The ratio was calculated at each increment of the corresponding analysis based on the Eqs. 4 and 5.

formulae available in the literature demonstrate that porosity is disproportionate with Young's modulus [27,28]. Thus, higher values of total porosity are linked with a reduction in stiffness. However, this applies only if the comparison is made on the same material. The black and brown LFCM sample materials described in this paper have similar, but not identical, compositions.

A more detailed study of the full-scale tomograms showed that the bottom surface of the brown LFCM sample was not perfectly flat. A representative 2D reconstructed slice, illustrating the full size of the sample, is given in Fig. 27. The corner lump present across the bottom surface of the sample has certainly affected its mechanical response, leading to a premature yielding during scanning. Therefore, it is believed that the load bearing capacity of the brown LFCM sample would be considerably higher. The fact that it is both more porous and stiffer compared to black LFCM hinders the possibility to estimate with confidence which of the two materials has a greater yield strength. The calculation of Young's modulus for the brown LFCM sample is not expected to be affected by the lump presence, since DVC calculations are only based on the relative movement of the features to determine sample deformation. The results from analyses conducted to determine the Poisson's ratio of the two materials showed that even among those values which lie within the range for a continuum (0 to 0.5), significant scattering was observed. It is believed that this behaviour is linked with the DVC volumes investigated as they contained significant volumes of porosity.

The Young's moduli determined for the black and brown LFCM samples via the DVC analysis ranged between approximately 5 GPa and 16 GPa. However, these values were calculated based on a uniaxial

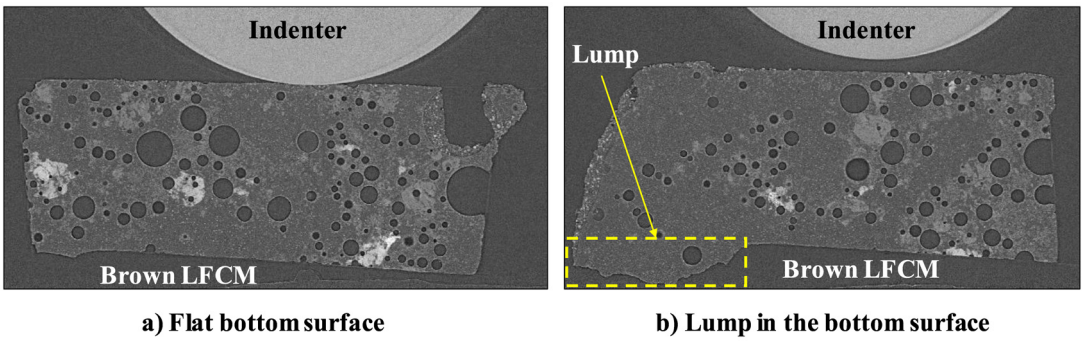

Fig. 27. Representative 2D reconstructed slices illustrating the local presence of a lump across the bottom surface of the brown LFCM sample material. Screenshots correspond to different sample regions at the same loading stage.

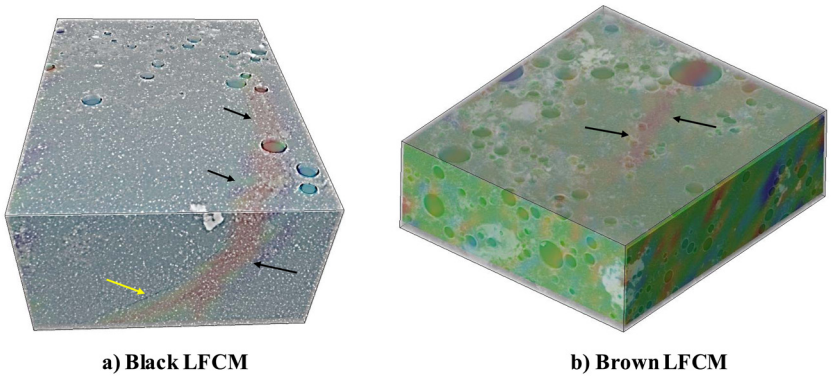

Fig. 28. Pre-loaded material volumes superimposed with relevant DVC strain maps for: a) black LFCM; b) brown LFCM. Yellow and black arrows demonstrate material discontinuities and elevated strain zones, respectively.

compression scenario, which differs from the Hertzian indentation methodology employed for testing in I12 beamline. This hypothesis was necessary to provide numerical solutions for the problem being studied. Additional FE modelling work was performed, targeted to estimate the effect of the uniaxial compression hypothesis on the realistic materials stiffness. The FE results suggested that the real Young's modulus of the black LFCM sample should be 28% higher than the corresponding value determined via the DVC analysis (Table 7). The corresponding percentage for the brown LFCM sample was 49%. This range of revised stiffness values (7 GPa to 24 GPa) seems comparable and compatible with the values of Young's modulus reported for a number of other brittle and quasi-brittle materials. Ceramics, glasses, and polymers are the most common groups of materials classified as brittle. Common ceramics include porcelain and bricks, whose typical Young's moduli are 7 GPa to 10 GPa and 3 GPa to 5 GPa, respectively. Other, less commonly used, brittle materials may display similar stiffness values (e.g. magnesium silicate: 4 GPa to 5 GPa) or even slightly greater (e.g. forsterite: 13 GPa to 15 GPa). Polymers are generally softer than ceramics. Most noticeably, Young's moduli of traditional polymers, such as nylon, acrylic, polystyrene, and polypropylene, lie within the range 1.3 GPa to 3.4 GPa. Generally, except for glass, which can display a wide variety of stiffness values, it could be concluded that a typical range of Young's modulus values for brittle materials ranges between 1 GPa and 15 GPa. However, the comparison described in the above paragraph was not given to indirectly prove that the Young's modulus values reported in this paper for the LFCM samples are correct. It is important to mention that a considerable minority of brittle materials exhibit significantly high stiffness. One typical example is zirconia (ZrO_2) which exhibits a Young's modulus value equal to 210 GPa.

Quasi-brittle materials differ from brittle ones since they display a softening behaviour after peak load instead of a sudden complete loss of load bearing capacity. Among common quasi-brittle materials, concrete and graphite are probably the most broadly investigated. A typical range of Young's modulus values for concrete could lie between 14 GPa and 41 GPa. Based on its composition, graphite stiffness is slightly lower (4 GPa to 28 GPa). Generally, the Young's modulus values calculated for black LFCM and brown LFCM, using the DVC data lie in good agreement with typical corresponding values reported for other brittle and quasi-brittle materials. Based on the sample loading behaviour (Fig. 2) it seems that there is no softening after the peak load. Thus, it could be safely confirmed that the two samples tested on the DLS I12 beamline are classifiable as brittle materials of slightly increased stiffness compared to the average. The displacement and strain maps created after performing the DVC analysis revealed zones of elevated deformation in locations where cracks formed after sample failure, as shown by the corresponding tomograms. The DVC maps and the tomograms related to the pre-failed status of the samples were combined to investigate potential correlation between the microstructure and the crack network formed after sample failure. Fig. 28 presents tomograms related to the first loading stage (11 N and 15 N for the black LFCM and the brown LFCM, respectively) superimposed with corresponding DVC strain maps (ε_{xy} and ε_{yy} strain for the black LFCM and the brown LFCM, respectively).

A narrow crack present within the black LFCM sample, which has formed during sample preparation (yellow arrow in Fig. 28a) and prior to loading, is very close and almost perfectly parallel to the zone of elevated strain, as shown from the corresponding DVC map. It is expected that this crack facilitated interior sample deformation. The orientation of the elevated strain zone (black arrows) around the upper surface of the cuboid in Fig. 28a shows that the presence of large pores has acted as a preference path for further deformation and potentially crack propagation. The brown LFCM sample volume (Fig. 28b) exhibited no obvious material discontinuities apart from pores being present. The elevated strain zone, as demonstrated by a red colour

strip (black arrows), contains several small pores along the length. It is interesting to note that no pores exist at the sides of this elevated strain zone, while a solid Si-rich matrix can be observed.

5. Conclusions

A combined investigation of the microstructure and mechanical behaviour of hazardous materials requiring retrieval from Chernobyl Unit 4 nuclear reactor power plant has been presented, using simulant samples. The methodology included a series of stepwise Hertzian indentation loading performed on surrogate materials, coupled with successive synchrotron XCT, and subsequently analysed using DVC. The goal was predominantly to determine the morphology, load bearing capacity and stiffness of the samples investigated. The key findings are summarised as follows:

- The combined Hertzian indentation-XCT-DVC methodology proved to be a successfully defined process to determine the mechanical behaviour of hazardous materials with sample volume restrictions during testing.
- Sample testing showed that the "lava" simulant materials can be classified as brittle with no evident softening behaviour.
- Brown LFCM exhibited almost two times greater general porosity than black LFCM (~12% compared to ~6%)
- DVC-based displacement and strain maps clearly revealed the zones of forthcoming excessive cracking before those appeared in the relevant tomograms.
- The range of Young's moduli calculated for the two samples tested on the DLS I12 beamline was approximately 7 GPa to 24 GPa.
- The different failure mechanisms noted for the two materials tested hinders the possibility to directly compare their load-bearing capacities.
- The brown LFCM sample stiffness was considerably higher than that of the black LFCM sample.

Data availability

The raw/processed data required to reproduce these findings cannot be shared at this time as the data also forms part of an ongoing study.

Declaration of Competing Interest

None.

Acknowledgements

The presented work is part of the CHIMP programme, funded by EPSRC. This research was a joint UK–Japan effort to support ongoing clean-up operations at the Fukushima Daiichi Nuclear Power Plant (funder reference: EP/R01924X/1). The authors would like to thank Diamond Light Source for awarding beamtime (EE20189-1) and the entire team of the DLS I12 beamline (Diamond Light Source) for supporting this research. M. Mostafavi acknowledges the support of the Royal Academy of Engineering through a Senior Research Fellowship and EPSRC (EPSRC grant number EP/R013047/1). C. Corkhill wishes to acknowledge EPSRC for funding through an Early Career Research Fellowship (EP/N017374/1). D. Liu and J. Forna-Kreutzer acknowledge EPSRC New Investigator Award (EP/T000368/1).

References

[1] A.A. Shiryaev, I.E. Vlasova, B.E. Burakov, B.I. Ogorodnikov, V.O. Yapaskurt, A.A. Averin, A.V. Pakhnevich, Y.V. Zubavichus, Physico-chemical properties of Chernobyl lava and their destruction products, Prog. Nucl. Energy 92 (2016) 104–118, https://doi.org/10.1016/j.pnucene.2016.07.001.
[2] B.Y. Zubekhina, B.E. Burakov, Leaching of actinides and other radionuclides from matrices of Chernobyl "lava" as analogues of vitrified HLW, J. Chem. Thermodyn. 114 (2017) 25–29, https://doi.org/10.1016/j.jct.2016.08.029.
[3] B.E. Burakov, E.B. Anderson, S.I. Shabalev, E.E. Strykanova, S.V. Ushakov, M. Trotabas, J.Y. Blanc, P. Winter, J. Duco, The behavior of nuclear fuel in first days of the Chernobyl accident, MRS Proc. 465 (1996) 1297, https://doi.org/10.1557/PROC-465-1297.
[4] B.E. Burakov, S.I. Shabalev, E.B. Anderson, Principal features of Chernobyl hot particles: phase, chemical and radionuclide compositions, Role Interf. Environ. Prot, Springer Netherlands (2003) 145–151, https://doi.org/10.1007/978-94-010-0183-0_10.
[5] I.E. Kuzmina, V.V. Tokarevskii, Sources and mechanisms of aerosol formation in the chernobyl "sarcophagus", At Energy 82 (1997) 129–135, https://doi.org/10.1007/BF02413463.
[6] A.A. Borovoi, Nuclear fuel in the shelter, At Energy 100 (2006) 249–256, https://doi.org/10.1007/s10512-006-0079-3.
[7] S.T. Barlow, D. Bailey, D.J. Fisher, C.L. Corkhill, N.C. Hyatt, Synthesis of simulant "lava-like" fuel containing materials (LFCM) from the Chernobyl reactor unit 4 meltdown, MRS Adv. (2016) 2–6, https://doi.org/10.1557/adv.2016.642.
[8] S.T. Barlow, D.J. Bailey, A.J. Fisher, M.C. Stennett, C. Gausse, H. Ding, V.A. Krasnov, S.Y. Sayenko, N.C. Hyatt, C.L. Corkhill, Synthesis, characterisation and corrosion behaviour of simulant Chernobyl nuclear meltdown materials, NPJ Mater. Degrad. 4 (2020) 1–8, https://doi.org/10.1038/s41529-020-0108-z.
[9] B.K. Bay, T.S. Smith, D.P. Fyhrie, M. Saad, Digital volume correlation: three-dimensional strain mapping using X-ray tomography, Exp. Mech. 39 (1999) 217–226, https://doi.org/10.1007/BF02323555.
[10] B.K. Bay, Methods and applications of digital volume correlation, J. Strain Anal. Eng. Des. 43 (2008) 745–760, https://doi.org/10.1243/03093247JSA436.
[11] A. Buljac, C. Jailin, A. Mendoza, J. Neggers, T. Taillandier-Thomas, A. Bouterf, B. Smaniotto, F. Hild, S. Roux, Digital volume correlation: review of progress and challenges, Exp. Mech. 58 (2018) 661–708, https://doi.org/10.1007/s11340-018-0390-7.
[12] B. Wang, L. Sun, B. Pan, Mapping internal deformation fields in 3D printed porous structure with digital volume correlation, Polym. Test. 78 (2019) 105945, https://doi.org/10.1016/J.POLYMERTESTING.2019.105945.
[13] M. Mostafavi, D.M. Collins, B. Cai, R. Bradley, R.C. Atwood, C. Reinhard, X. Jiang, M. Galano, P.D. Lee, T.J. Marrow, Yield behavior beneath hardness indentations in ductile metals, measured by three-dimensional computed X-ray tomography and digital volume correlation, Acta Mater. 82 (2015) 468–482, https://doi.org/10.1016/J.ACTAMAT.2014.08.046.
[14] Y. Vertyagina, M. Mostafavi, C. Reinhard, R. Atwood, T.J. Marrow, In situ quantitative three-dimensional characterisation of sub-indentation cracking in polycrystalline alumina, J. Eur. Ceram. Soc. 34 (2014) 3127–3132, https://doi.org/10.1016/J.JEURCERAMSOC.2014.04.002.
[15] M. Mostafavi, N. Baimpas, E. Tarleton, R.C. Atwood, S.A. McDonald, A.M. Korsunsky, T.J. Marrow, Three-dimensional crack observation, quantification and simulation in a quasi-brittle material, Acta Mater. 61 (2013) 6276–6289, https://doi.org/10.1016/J.ACTAMAT.2013.07.011.
[16] Z. Yang, W. Ren, R. Sharma, S. McDonald, M. Mostafavi, Y. Vertyagina, T.J. Marrow, In-situ X-ray computed tomography characterisation of 3D fracture evolution and image-based numerical homogenisation of concrete, Cem. Concr. Compos. 75 (2017) 74–83, https://doi.org/10.1016/J.CEMCONCOMP.2016.10.001.
[17] M. Mostafavi, S.A. McDonald, P.M. Mummery, T.J. Marrow, Observation and quantification of three-dimensional crack propagation in poly-granular graphite, Eng. Fract. Mech. 110 (2013) 410–420, https://doi.org/10.1016/j.engfracmech.2012.11.023.
[18] B.E. Burakov, E.E. Strykanova, E.B. Anderson, Secondary uranium minerals on the surface of Chernobyl "lava", MRS Proc. 465 (1997) 1309, https://doi.org/10.1557/PROC-465-1309.
[19] P. Pöml, B. Burakov, T. Geisler, C.T. Walker, M.L. Grange, A.A. Nemchin, J. Berndt, R.O.C. Fonseca, P.D.W. Bottomley, R. Hasnaoui, Micro-analytical uranium isotope and chemical investigations of zircon crystals from the Chernobyl "lava" and their nuclear fuel inclusions, J. Nucl. Mater. 439 (2013) 51–56, https://doi.org/10.1016/J.JNUCMAT.2013.03.031.
[20] L. Saucedo-Mora, M. Mostafavi, D. Khoshkhou, C. Reinhard, R. Atwood, S. Zhao, B. Connolly, T.J. Marrow, Observation and simulation of indentation damage in a SiC-SiC fibre ceramic matrix composite, Finite Elem. Anal. Des. 110 (2016) 11–19, https://doi.org/10.1016/j.finel.2015.11.003.
[21] M. Drakopoulos, T. Connolley, C. Reinhard, R. Atwood, O. Magdysyuk, N. Vo, M. Hart, L. Connor, B. Humphreys, G. Howell, S. Davies, T. Hill, G. Wilkin, U. Pedersen, A. Foster, N. De Maio, M. Basham, F. Yuan, K. Wanelik, I12: the joint engineering, environment and processing (JEEP) beamline at diamond light source, J. Synchrotron Radiat. 22 (2015) 828–838, https://doi.org/10.1107/S1600577515003513.
[22] R.C. Atwood, A.J. Bodey, S.W.T. Price, M. Basham, M. Drakopoulos, A high-throughput system for high-quality tomographic reconstruction of large datasets at diamond light source, Philos. Trans. R. Soc. A Math. Phys. Eng. Sci. 373 (2015) 20140398, https://doi.org/10.1098/rsta.2014.0398.
[23] AVIZO, AVIZO User's Guide, 2018.
[24] T. Ferreira, W. Rasband, ImageJ User Guide 1.46r, 2012.
[25] S.M. Barhli, L. Saucedo-Mora, M.S.L. Jordan, A.F. Cinar, C. Reinhard, M. Mostafavi, T.J. Marrow, Synchrotron X-ray characterization of crack strain fields in polygranular graphite, Carbon N. Y. 124 (2017) 357–371, https://doi.org/10.1016/j.carbon.2017.08.075.
[26] ABAQUS, User's Manual Version 6.14, Providence, RI, USA, 2014.
[27] J. Kováčik, Correlation between Young's modulus and porosity in porous materials, J. Mater. Sci. Lett. 18 (1999) 1007–1010, https://doi.org/10.1023/A:1006669914946.
[28] K.K. Phani, S.K. Niyogi, Young's modulus of porous brittle solids, J. Mater. Sci. 22 (1987) 257–263, https://doi.org/10.1007/BF01160581.